Application of approximate dispersion-diffusion analyses to under-resolved Burgers turbulence using high resolution WENO and UWC schemes

P. Solán-Fustero*, A. Navas-Montilla*¶§, E. Ferrer †‡, J. Manzanero†‡, P. García-Navarro*

Abstract

This paper presents a space-time approximate dispersion-diffusion analysis of high-order, finite volume Upwind Central (UWC) and Weighted Essentially Non-Oscillatory (WENO) schemes. We perform a thorough study of the numerical errors to find a-priori guidelines for the computation of under-resolved turbulent flows. In particular, we study the 3-rd, 5-th and 7-th order UWC and WENO reconstructions in space, and 3-rd and 4-th order Runge-Kutta time integrators. To do so, we use the approximate von Neumann analysis for non-linear schemes introduced by Pirozzoli. Moreover, we apply the "1% rule" for the dispersion-diffusion curves proposed by Moura et al. [41] to determine the range of wavenumbers that are accurately resolved by each scheme. The dispersion-diffusion errors estimated from these analyses agree with the numerical results for the forced Burgers' turbulence problem, which we use as a benchmark. The cut-off wavenumbers defined by the "1% rule" are evidenced to serve as a good estimator of the beginning of the dissipation region of the energy cascade and they are shown to be associated to a similar level of dissipation, with independence of the scheme.

Finally, we show that WENO schemes are more diffusive than UWC schemes, leading to stable simulations at the price of more dissipative results. It is concluded both UWC and WENO schemes may be suitable schemes for iLES turbulence modelling, given their numerical dissipation level acting at the appropriate wavenumbers.

Keywords: Dispersion-diffusion analysis; von Neumann; High-order schemes; Weighted Essentially Non-Oscillatory WENO; Burgers' turbulence; implicit Large Eddy Simulation

Contents

*Fluid Mechanics Department-Aragon Institute of Engineering Research (I3A), Universidad de Zaragoza-CSIC.

¶Centro Universitario de la Defensa, Carretera de Huesca s/n, E-50090 Zaragoza, Spain.

†ETSIAE-UPM - School of Aeronautics, Universidad Politécnica de Madrid.

‡Center for Computational Simulation, Universidad Politécnica de Madrid.

§Corresponding author (anavas@unizar.es)

1. Introduction

In recent years, the scientific community has started to favour numerical schemes with high accuracy [4, 9, 20], which are often referred to as high order methods (i.e. order > 2). Examples of high order schemes include Upwind Central (UWC), Weighted Essentially Non-Oscillatory (WENO) or discontinuous Galerkin, which can be combined with compact time integration: Runge-Kutta (RK) or ADER methods [14, 17, 42, 43, 53], to feature low numerical errors and construct accurate high order space-time numerical schemes. Details on high order methods may be found in the review of WENO schemes by Shu [52] or by Balsara [3], who studied various higher-order accurate space-time schemes (including WENO, discontinuous Galerkin and ADER schemes). There are also several works on improving the efficiency of WENO schemes, such as Jiang and Shu [27] and Balsara et al. [5], in which the adaptive order WENO schemes (WENO-AO) are presented. The 7-th order WENO schemes used in this work were first presented by Balsara and Shu in [6].

High-order schemes are exceptional candidates for the computation of laminar flows but are also very useful to simulate under-resolved turbulent flows due to their compromise between high accuracy and efficiency [18, 23, 32]. WENO schemes are an example of well behaved scheme for all class of flows, since in smooth regions, WENO recovers highly accurate central stencils, whilst for non-smooth flows, the embedded smoothness indicator allows for reconstructions that find the smoothest one-sided stencil.

All numerical schemes unavoidably introduce errors in the numerical solution, which can be divided into dispersion and diffusion errors [49]. To quantify the accuracy of numerical methods, Fourier-type analyses have proved very useful in the past [38, 41, 44], and can shed light into more complex physics such as when dealing with turbulent flows. Additionally, an in depth knowledge of the numerical errors help to design or

validate numerical schemes used to simulate turbulent flows [11, 37]. The Fourier-type analysis proposed by von Neumann [13, 25] establishes a dispersion-diffusion relation as a function of the Fourier mode's wavenumber. This analytical procedure can only be applied to linear equations and linear numerical schemes. For non-linear approximations, Pirozzoli [44] proposed a suitable approximate dispersion relation for non-linear shock-capturing schemes based on their wave propagation properties for smooth solutions. Pirozzoli's approach will be retained in this work to analyse the characteristics of non-linear WENO schemes. Additionally, Fourier-type analyses enable the estimation of a cut-off wavenumber from which numerical diffusion dominates. In this respect, Moura et al. [41] proposed the "1% rule" to estimate the effective resolution of the numerical scheme in terms of the largest wavenumber that can be accurately resolved, $k_{1\%}$ (i.e. wavenumbers with error smaller than 1%). Subsequently, this technique has been used to design accurate schemes for implicit Large Eddy Simulations [11, 37].

Implicit Large Eddy Simulation (iLES) methods encompass schemes where the numerical diffusion plays the role of the explicit dissipative sub-grid model. Although it is still not clear, from a theoretical perspective, if the numerical diffusion can accurately retain the underlying physics, iLES methods have been successful in capturing the correct physics for turbulent and transitional flows [8, 15, 54, 19, 55]. Among the advantages, we highlight the simplicity and the low computational cost when compared to explicit LES models, as they do not require the computation of a sub-grid model [41].

In classic low order schemes, spatial errors dominate over temporal errors as usually the characteristic mesh size is larger than the time step. This tendency changes when considering high order spatial schemes, since in these cases spatial and temporal errors can become comparable. The analysis of dispersion-diffusion errors is commonly carried out semi-discretely, assuming that the integration in time does not introduce large errors (compared to spatial errors) given a small enough time step [2, 38, 40, 48, 47], however full space-time analysis are possible and of major importance when dealing with high order discretizations, as included in this text. Further arguments in favour of space-time analyses were introduced by Alhawwary and Wang in [1], who stated that time integrators introduce significant numerical diffusion in iLES simulations, as one usually chooses the highest time step available under the CFL stability constraint.

In the literature, the Fourier-type analysis is generally applied to linear advection equations, to then validate the observations in more challenging applications, such as non-linear regimes. An example is Burgers' turbulence, which consists in solving Burgers' equation [10, 16] with either a turbulent forcing term or a turbulent initial condition. This equation acts as simplified version of the one-dimensional Navier-Stokes equation, while retaining important properties like quadratic nonlinearities leading to turbulent-like energy cascades [30, 35, 40, 41].

In this work we analyze several fully-discrete, high-order finite volume schemes by means of the approximate dispersion-diffusion analysis [44] and the "1% rule" [11, 37, 41] to obtain a-priori guidelines for suitable computation of under-resolved turbulence. The results obtained from the approximate dispersion-diffusion analysis are compared to forced Burgers' turbulence results [38].

The selected numerical schemes for this study are the 3-rd, 5-th and 7-th order UWC and WENO reconstructions (namely, the traditional WENO reconstruction from Jiang and Shu, often called WENO-JS [27]) in combination with 3-rd and 4-th order Runge-Kutta time integrators. WENO schemes, originally presented by Liu et al. [34], are of special interest due to their capability to accurately capture both discontinuous and

smooth regions of the flow, without spurious oscillations [50]. The keystone of such schemes is a dynamic stencil selection, based on a measure of the smoothness of the solution. Those stencils containing discontinuities are not included in the reconstruction and the accuracy is reduced to first order. It must be noted that UWC schemes are the linear counterpart of WENO schemes, for which the linear weights are recovered in the stencil combination.

There is an extensive literature regarding the evaluation of the properties of different WENO schemes for their application to wave propagation problems and compressible Navier-Stokes turbulence. Even though WENO schemes are regarded as very diffusive, specially in smooth regions [28, 33], they have been considered for iLES simulations, where the role of a SGS model is replaced by the numerical scheme [22, 39, 40, 46, 57]. There are not many studies where the analysis is applied to the fully-discrete scheme including the integration in time. Here, we use the "1% rule" to provide a new systematic way to evaluate UWC-RK and WENO-RK schemes in fully non-linear problems, and extend von Neumann analyses to quantify the accuracy of high order schemes in turbulent-like regimes. The application of the analysis and results herein presented to CFD simulations could be a useful tool for engineers, as it would help to select the numerical scheme in terms of spatial reconstruction type and order, time integration order and/or CFL number, for a given problem and a sought accuracy and efficiency.

The rest of the paper is organized as follows: the formulation of the UWC-RK and WENO-RK methods is described in Section 2. The Fourier-type analysis is presented in Section 3, in both analytical and approximate versions, and the cut-off wavenumbers given by the "1% rule" are examined. In Section 4.2, the values obtained from the "1% rule" are tested against the results of the forced Burgers' turbulence problem, showing the performance of UWC/WENO-RK schemes. Finally, in Section 5 some conclusions are drawn.

2. High order numerical schemes

The methods considered herein focus on the resolution of the one dimensional scalar hyperbolic law,

$$\frac{\partial u}{\partial t} + \frac{\partial f(u)}{\partial x} = S(x,t), \tag{1}$$

where $u = u(x,t) \in \mathcal{C} \subseteq \mathbb{R}$ is the conserved quantity, with $\mathcal{C}$ the domain; $f(u) \in \mathbb{R}$ is a convex flux function; and $S(x,t) \in \mathbb{R}$ is the source term. Following the finite volume method, the computational domain is discretized by means of volume cells (considered of constant length, Δx, in this work) as seen in Figure 1. The discretization cells are defined as $\Omega_j = \left[x_{j-1/2}, x_{j+1/2}\right]$ (with $j = 1, ..., N$, being $N \in \mathbb{N}$ the number of cells), where x_j, $x_{j-1/2}$ and $x_{j+1/2}$ are the positions of the center and interfaces of cell Ω_j, respectively. The time step will be denoted by Δt and will be computed dynamically using the CFL condition [13, 25].

When integrating 1 inside Ω_j,

$$\int_{x_{j-1/2}}^{x_{j+1/2}} \frac{\partial u}{\partial t} dx + \int_{x_{j-1/2}}^{x_{j+1/2}} \frac{\partial f(u)}{\partial x} dx = 0, \tag{2}$$

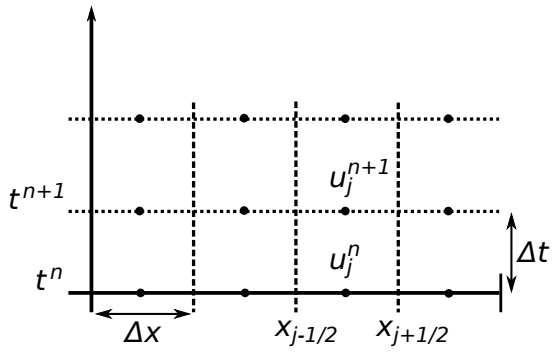

Figure 1: Discretized computational domain.

we get a semidiscrete form of (1),

$$\frac{\mathrm{d}\bar{u}_j}{\mathrm{d}t} - \frac{1}{\Delta x}\left(\tilde{f}^{\star}_{j+1/2} - \tilde{f}^{\star}_{j-1/2}\right) = 0, \tag{3}$$

where $\bar{u}_j$ is the cell-averaged value of u and $\tilde{f}^{\star}_{j+1/2}$ and $\tilde{f}^{\star}_{j-1/2}$ are the numerical fluxes at the interfaces, that approximate $f(u)$. Making use of the discrete spatial operator, $\mathcal{L}(\bar{u}_j)$, (3) can be compactly written as

$$\frac{\mathrm{d}\bar{u}_j}{\mathrm{d}t} = \mathcal{L}(\bar{u}_j), \tag{4}$$

with

$$\mathcal{L}(\bar{u}_j) = \frac{1}{\Delta x}\left(\tilde{f}^{\star}_{j+1/2} - \tilde{f}^{\star}_{j-1/2}\right). \tag{5}$$

We integrate in time using a strong stability preserving third-order Total Variation Diminishing Runge-Kutta (TVDRK3) scheme [47], hereafter referred to as RK3, composed of three sub-steps,

$$\begin{aligned}
\bar{u}_j^{(1)} &= \bar{u}_j^n + \Delta t\mathcal{L}(\bar{u}_j^n),\\
\bar{u}_j^{(2)} &= \tfrac{3}{4}\bar{u}_j^n + \tfrac{1}{4}\bar{u}_j^{(1)} + \tfrac{1}{4}\Delta t\mathcal{L}(\bar{u}_j^{(1)}),\\
\bar{u}_j^{n+1} &= \tfrac{1}{3}\bar{u}_j^n + \tfrac{2}{3}\bar{u}_j^{(2)} + \tfrac{2}{3}\Delta t\mathcal{L}(\bar{u}_j^{(2)}),
\end{aligned} \tag{6}$$

where $\bar{u}_j^n$ and $\bar{u}_j^{n+1}$ are cell-averaged values at times t^n and t^{n+1}, respectively, and $\bar{u}_j^{(1)}$ and $\bar{u}_j^{(2)}$ the cell averaged values in the RK3 intermediate steps.

Since the temporal accuracy of the 3-rd order RK time stepping scheme does compete with the spatial accuracy when using the 5-th and 7-th order scheme with a high CFL number, a SSP 4-th order RK scheme [24] has also been implemented. This scheme,

hereafter referred to as RK4, is composed of five sub-steps

$$
\begin{aligned}
\bar{u}_j^{(1)} &= \bar{u}_j^n + 0.391752226571890\Delta t\mathcal{L}(\bar{u}_j^n),\\
\bar{u}_j^{(2)} &= 0.444370493651235\bar{u}_j^n + 0.555629506348765\bar{u}_j^{(1)} + 0.368410593050371\Delta t\mathcal{L}(\bar{u}_j^{(1)}),\\
\bar{u}_j^{(3)} &= 0.620101851488403\bar{u}_j^n + 0.379898148511597\bar{u}_j^{(2)} + 0.251891774271694\Delta t\mathcal{L}(\bar{u}_j^{(2)}),\\
\bar{u}_j^{(4)} &= 0.178079954393132\bar{u}_j^n + 0.821920045606868\bar{u}_j^{(3)} + 0.544974750228521\Delta t\mathcal{L}(\bar{u}_j^{(3)}),\\
\bar{u}_j^{n+1} &= 0.517231671970585\bar{u}_j^{(2)} + 0.096059710526147\bar{u}_j^{(3)} + 0.063692468666290\Delta t\mathcal{L}(\bar{u}_j^{(3)})\\
&\quad +0.386708617503269\bar{u}_j^{(4)} + 0.226007483236906\Delta t\mathcal{L}(\bar{u}_j^{(4)}),
\end{aligned}
\tag{7}
$$

We use upwind fluxes to compute the numerical inter-cell fluxes,

$$
\tilde{f}^{\star}_{j+1/2} = \frac{1}{2}\left(f^R_{j+1/2} + f^L_{j+1/2}\right) - (\tilde{\lambda}\Delta u)_{j+1/2}, \tag{8}
$$

where $f^L_{j+1/2} = f(u^L_{j+1/2})$ and $f^R_{j+1/2} = f(u^R_{j+1/2})$ are the physical fluxes, $\tilde{\lambda}_{j+1/2}$ is the local wave propagation speed,

$$
\tilde{\lambda}_{j+1/2} = \left.\frac{\partial f(u)}{\partial u}\right|_{j+1/2}, \tag{9}
$$

and $\Delta u_{j+1/2} = u^R_{j+1/2} - u^L_{j+1/2}$. The values $u^L_{j+1/2}$ and $u^R_{j+1/2}$ are computed using high-order reconstructions in space. In this work, we use WENO schemes, which define the reconstructed data at the interfaces from a piecewise reconstructions inside the cells. WENO reconstructions at the left and right interfaces of cell j read [34]

$$
\begin{aligned}
u^L_{j+1/2} &= \sum_{m=1}^{(K+1)/2} \omega^L_m \left[\sum_{n=1}^{(K+1)/2} c^L_{mn}\bar{u}_{j+m-n}\right],\\
u^R_{j-1/2} &= \sum_{m=1}^{(K+1)/2} \omega^R_m \left[\sum_{n=1}^{(K+1)/2} c^R_{mn}\bar{u}_{j+m-n}\right],
\end{aligned}
\tag{10}
$$

where K is the (odd) spatial order of accuracy. For the sake of simplicity, superscripts L and R are hereafter omitted. The non-linear weights ω_m, both for left and right values, are

$$
\omega_m = \frac{\alpha_m}{\sum_{i=1}^{(K+1)/2}\alpha_i}, \qquad m = 1, ..., (K+1)/2, \tag{11}
$$

with the coefficients α_m,

$$
\alpha_m = \frac{d_m}{(\beta_m + \epsilon)^2}, \qquad m = 1, ..., (K+1)/2. \tag{12}
$$

The optimal linear weights, d_m, and the smoothness indicators, β_m, are provided in Appendix A, as well as the coefficients c_{mn}; ϵ is given a small value to eliminate divisions by zero. The value $\epsilon = 10^{-14}$ is retained here. Note that when (12) is not used, and if setting $\alpha_m = d_m$, then the linear Upwind Central scheme (UWC) is recovered [51]. In

this work we study both the WENO (non-linear reconstruction) and the UWC (linear reconstruction) schemes, which are compared to a first-order upwind scheme (FOU) [21, 31].

It must be noted that in this paper we restrict to the traditional WENO scheme by Jiang and Shu [27]. However, recent improvements of the WENO method have been introduced, such as the adaptive order WENO scheme (WENO-AO) presented in [5], which allows to approach the behavior of UWC schemes in some limits, thus improving the efficiency of the method.

3. Methodologies for dispersion-diffusion analyses

The numerical approximation of the 1D linear advection equation 1 usually involves the presence of spurious dispersive and diffusive effects in the numerical solution. When dealing with linear numerical schemes, such as UWC and FOU schemes, the traditional von Neumann analysis gives the analytical expression for the numerical dispersion and diffusion [13, 25]. Alternatively, an approximate dispersion-diffusion relation can be defined for non-linear schemes, such as the WENO method, using the technique proposed in [44]. Following [44], the spectral properties of the aforementioned schemes will be extracted by analyzing the evolution of a single sinusoidal wave, from a finite set of wavenumbers within the Fourier modes supported by the grid. Let us note that a simplification is made for the non-linear cases in that non-linear interactions between waves with different wavenumbers will not be taken into account.

We analyse the propagation of small perturbations to obtain the analytical and/or approximate dispersion-diffusion relation for a linear scheme (the UWC scheme) and a non-linear scheme (the WENO scheme) in combination with the RK3 integrator.

We use the 1D linear advection equation, given by the homogeneous version of equation (1), with the particular flux $f(u) = au$, where a is a constant advection velocity. Space and time coordinates are denoted by x and t, respectively. The computational domain is defined as $\Omega \times [0, T]$, where T is the simulation time and $\Omega = [-L, L]$ is the spatial domain, with $T, L \in \mathbb{R}^+$. To avoid boundary effects, periodic boundary conditions are considered, i.e. $u(-L, t) = u(L, t)$. As initial condition, one single oscillatory mode $u(x, 0) = \hat{u}_k e^{i(kx)}$ is set, where $k = 2\pi/\lambda$ is the wavenumber, λ is the wavelength and $\hat{u}_k$ is the amplitude of the k-th Fourier mode,

$$\hat{u}_k = \frac{1}{2L} \int_{-L}^{L} u(x) e^{-i(kx)} \mathrm{d}x. \tag{13}$$

The exact solution of the 1D linear advection equation, with velocity a, at an arbitrary time t, is therefore

$$u(x, t) = \hat{u}_k e^{ik(x-at)}. \tag{14}$$

We have obtained a linear dispersion relation $\omega = ak$ for 1, with the angular frequency $\omega = 2\pi/T$ and the oscillation period T. The exact solution does not show dispersive characteristics since all modes propagate with speed a.

Contrary to the exact solution, the numerical solution may suffer from artificial diffusion and dispersion. The dispersion relation can generally be written as

$$\tilde{\omega}(\tilde{k}) = \tilde{k} a(\tilde{k}) = \xi + i\eta, \tag{15}$$

where $\tilde{\omega}$ is the modified angular frequency [25]. The advection velocity is then extended to $a = a(\tilde{k})$, with $\tilde{k} \in \mathbb{R}$, the modified wavenumber defined as the ratio between the modified angular frequency and the advection speed [41].

The numerical solution of 1 is generally expressed as

$$\bar{u}_j^n = \hat{u}_k e^{i(kj\Delta x - \tilde{\omega} n \Delta t)}, \tag{16}$$

where $\bar{u}_j^n$ are the cell averages at t^n, $x_j = j\Delta x$ are the cell centers and $t^n = n\Delta t$ the discrete time instants. For the sake of clarity, the top-bar notation will be hereafter omitted. Algebraic manipulations of the previous relation allows to define the amplification factor between the numerical solution at two successive time steps, $u_j^{n+1} = \mathcal{M} u_j^n$, as

$$\mathcal{M} = e^{-i\tilde{\omega}\Delta t} = e^{-i\xi\Delta t} e^{\eta \Delta t}, \tag{17}$$

This amplification factor can be written in polar form as $\mathcal{M} = |\mathcal{M}|\, e^{-i\theta}$, where $|\mathcal{M}| = e^{\eta \Delta t}$ is the magnitude of the amplification factor and $\theta = \xi \Delta t$ is the phase, which are related to diffusion (numerical dissipation) and dispersion (phase velocity differences), respectively.

The amplification factor $\mathcal{M}$ can be computed analytically to obtain the dispersion and diffusion relation provided that the numerical scheme is linear. Since here we consider non-linear numerical schemes, an approximate dispersion-diffusion relation has to be used instead, as explained in the following section.

3.1. Approximate dispersion-diffusion relation

The approximate dispersion-diffusion relation in [44] analyses the wave propagation properties of single sinusoidal modes by means of the Fourier Transform (FT) [1, 26, 38, 41, 44]. On a finite grid of length L and cells $j = 1, ..., N$ the supported Fourier modes have wavelengths $\lambda_m = L/m$, $m = 1, ..., N/2$ and the corresponding reduced wavenumbers are $\varphi_m = m\,(k\Delta x)$, with $0 \leq \varphi_m \leq \pi$. The quantity $k\Delta x$ is defined as the product of the signal wavenumber, k, and the elements size, Δx, to avoid the dependence with the domain length and the cells size. To analyze the full Fourier spectrum, we define a discrete set of modes, denoted by $\{\varphi_m\}$. This set is defined keeping a constant wavelength $\lambda = 2\pi$ [44],

$$\varphi_m = \frac{2\pi m}{N}, \quad m = 1, 2, ..., N/2. \tag{18}$$

The discrete solution computed by means of the the Discrete Fourier Transform (DFT) is

$$U_m^n = \frac{1}{N} \sum_{j=1}^{N} u_j^n e^{-i\frac{2\pi(j-1)m}{N}}, \quad m = 1, ..., N, \tag{19}$$

where U_m^n are the Fourier coefficients and m stands for the discrete Fourier mode index.

The approximate analysis starts by applying the DFT to the initial condition, where only the fundamental mode is obtained. According to (17) and [44], the relation between the Fourier coefficients of the initial condition, U_m^0, and the solution at an arbitrary time t^n, U_m^n, is

$$U_m^n = U_m^0 e^{-i\left(\frac{a t^n}{\Delta x}\right)\tilde{W}}, \tag{20}$$

where U_m^0 is the DFT of the cell averaged initial condition, $u_j^0 = \int_{x_{j-1/2}}^{x_{j+1/2}} u(x, t=0)dx$, following equation (19); and where $\mathcal{M}' = e^{-i(at^n/\Delta x)\tilde{W}}$ is the approximate amplification factor [26, 44], and $\tilde{W}$ is the approximate modified (non-dimensional) wavenumber. In the particular case with $n = 1$ and $t = \Delta t$, the amplification factor becomes

$$\mathcal{M}' = e^{-i\sigma\tilde{W}}, \tag{21}$$

which is related to (15) as $\tilde{\omega}\Delta t = \sigma\tilde{W}$, where $\sigma = a\Delta t/\Delta x$ is the CFL number. From (20), the approximate modified wavenumber is calculated as

$$\tilde{W} = -\frac{1}{i\sigma}\ln\frac{U_h^1}{U_h^0} = \Xi + iE. \tag{22}$$

Table 1 shows the equivalence of the dispersion and diffusion relations between analytical and approximate Fourier-type analyses.

	Dispersion ($\tilde{k}\Delta x$)	Diffusion ($\lvert\mathcal{M}\rvert$)
Analytical	$\xi\Delta t/\sigma \equiv \theta/\sigma$	$e^{\eta\Delta t}$
Approximate	Ξ	$e^{\sigma E}$

Table 1: Dispersion and diffusion relations for the analytical and approximate methods.

3.2. Error quantification using the "1% rule"

In this work, we revisit the "1% rule" introduced by Moura in [41] and exploited in [11, 37] in the context of DG and Lattice-Boltzmann schemes. The 1% rule consists in an estimation of which set of wavenumbers values can provide accurate wave propagation characteristics.

The "1% rule" is herein explored in the framework of UWC and WENO schemes. Originally, the "1% rule" wavenumber, $k_{1\%}$, was defined in [41] as an estimation of the largest wavenumber that can be accurately resolved. The underlying idea is to define a threshold for the waves where the relative dispersion errors are kept below the 1%. The information provided by the "1% rule" may be exploited to design suitable numerical schemes for iLES since, as argumented in [11, 37, 41], all waves with wavenumbers above the 1% limit should be dissipated as they may pollute the solution.

In this work, the definition of the $(k\Delta x)_{1\%}$ is extended from dispersion errors to both dispersion and diffusion relations, hereafter denoted by $(k\Delta x)_{1\%}^{\text{disp}}$ and $(k\Delta x)_{1\%}^{\text{diff}}$. The wavenumber $(k\Delta x)_{1\%}^{\text{disp}}$ differentiates between regions of negligible ($k\Delta x < (k\Delta x)_{1\%}^{\text{disp}}$) and significant ($k\Delta x > (k\Delta x)_{1\%}^{\text{disp}}$) dispersion relative errors. Analogously, $(k\Delta x)_{1\%}^{\text{diff}}$ differentiates between regions of negligible ($k\Delta x < (k\Delta x)_{1\%}^{\text{diff}}$) and significant ($k\Delta x > (k\Delta x)_{1\%}^{\text{diff}}$) diffusion relative errors. The aforementioned diffusion and dispersion relative errors are computed as:

$$\begin{aligned} \varepsilon_{1\%}^{\text{diff}} &= \left|\left|M\right|_{(k\Delta x)_{1\%}^{\text{disp}}} - 1\right| \\ \varepsilon_{1\%}^{\text{disp}} &= \left|\frac{\tilde{k}\Delta x\big|_{(k\Delta x)_{1\%}^{\text{diff}}} - (k\Delta x)_{1\%}^{\text{diff}}}{(k\Delta x)_{1\%}^{\text{diff}}}\right|. \end{aligned} \tag{23}$$

The analyses included in this work have been designed to assess the suitability of UWC and WENO schemes for the simulation of turbulent flows. Although further 3D turbulent cases need to be considered before definitively determining the suitability of the schemes to compute complex turbulent flows (e.g. wall bounded), the study does provide preliminary guidelines based on the dispersion-diffusion relation that help to predict the a-priori performance and suitable resolution for these schemes.

3.3. Mesh convergence study

Since the method of Pirozzoli [44] is approximate, the results depend on the mesh resolution. Therefore, we first perform a grid convergence analysis to rule out the effect of the mesh resolution (N in (18)) in the results of the approximate dispersion-diffusion errors. The convergence with mesh refinement (N = 4096, 8192 and 16384) of the diffusion and dispersion relative errors, $\varepsilon^{\text{diff}}_{1\%}$ and $\varepsilon^{\text{disp}}_{1\%}$, associated to $(k\Delta x)_{1\%}$ is studied in Figure 2 for the UWC3-RK3 scheme. We see that the diffusion error converges rapidly, thus not requiring a large number of cells. On the contrary, the asymptotic range of convergence for the dispersion relative error starts at $N \approx 4000$ cells. Therefore, from now on, all results are calculated using N = 8192 cells to avoid the dependency of $(k\Delta x)^{\text{disp}}_{1\%}$ and $(k\Delta x)^{\text{diff}}_{1\%}$ on the cells size.

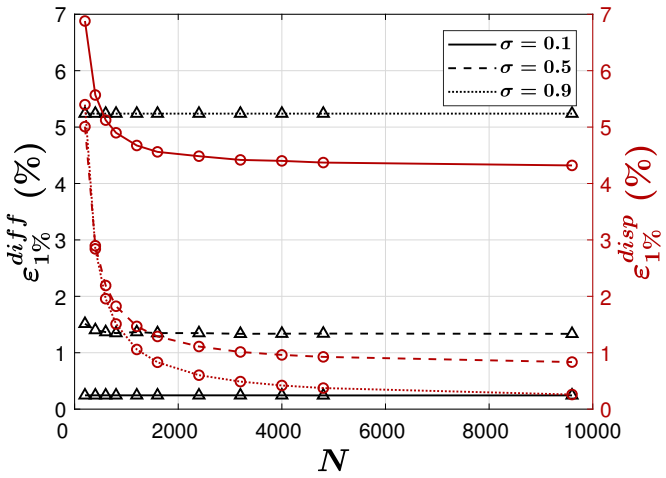

Figure 2: Convergence of the diffusion and dispersion errors with mesh refinement for UWC3-RK3, values: $\varepsilon^{\text{diff}}_{1\%}$ ($\sigma = 0.1$) (—◯—), $\varepsilon^{\text{diff}}_{1\%}$ ($\sigma = 0.5$) (- -◯- -), $\varepsilon^{\text{diff}}_{1\%}$ ($\sigma = 0.9$) (···◯···), $\varepsilon^{\text{disp}}_{1\%}$ ($\sigma = 0.1$) (—△—), $\varepsilon^{\text{disp}}_{1\%}$ ($\sigma = 0.5$) (- -△- -) and $\varepsilon^{\text{disp}}_{1\%}$ ($\sigma = 0.9$) (···△···)

Additionally, we also validate the approximate method using the results for the WENO5 scheme by Jia et al. [26]. We confirm that our results show good agreement with the reference [26], both represented in Figure 3.

4. Numerical Results

We proceed to analyse the described FOU, UCW and WENO schemes using the linear advection equation and Burger's turbulence problem.

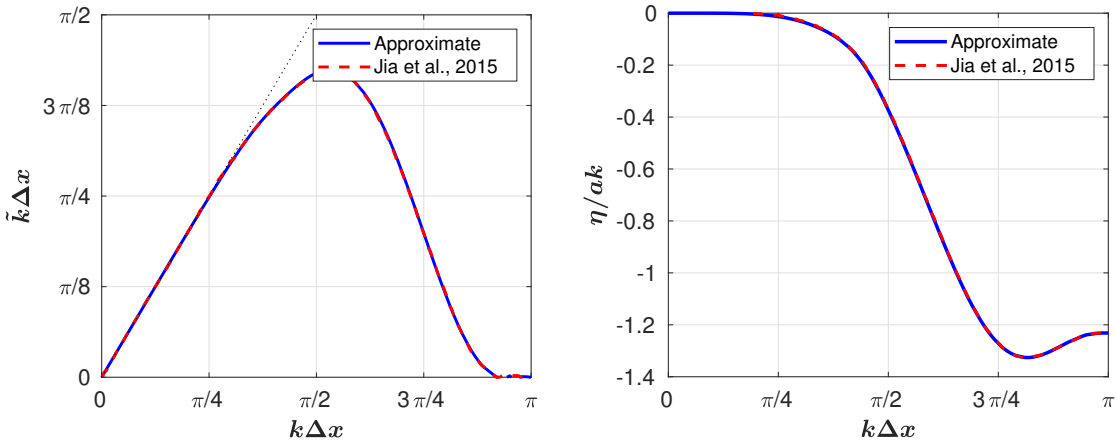

(a) Dispersion. (b) Diffusion.

Figure 3: Comparison of the approximate dispersion-diffusion relation with results from [26]. The ideal dispersion relation is depicted using a dashed line.

4.1. Numerical errors for the advection equation

The dispersion curves for the 3-rd, 5-th and 7-th order UWC and WENO schemes in combination with the RK3 and RK4 time integrators are presented in Figure 4. Analogously, the diffusion curves are presented for these schemes in Figure 5. Both RK3 and RK4 time integrators show similar dispersion-diffusion relations; differences are observed as the CFL number approaches 1. From these figures, it is inferred that dispersion errors behave similarly for all CFL numbers, σ. Contrarily, diffusion errors show larger differences between the different values of the CFL number. The numerical diffusion increases as σ is increased for both UWC and WENO schemes. As stated in previous works, WENO schemes involve a higher dispersive and diffusive errors than their linear counterparts.

In Table 2 and Table 3, $(k\Delta x)^{\text{disp}}_{1\%}$ and $(k\Delta x)^{\text{diff}}_{1\%}$ are presented for all the spatial schemes in combination with the RK3 and RK4 time integrators. The relative diffusion and dispersion errors associated to such wavenumbers, $\varepsilon^{\text{diff}}_{1\%}$ and $\varepsilon^{\text{disp}}_{1\%}$, are also presented in the tables 2 and 3.

Figure 6 displays the cut-off wavenumbers, $(k\Delta x)^{\text{disp}}_{1\%}$ and $(k\Delta x)^{\text{diff}}_{1\%}$. For low CFL numbers, i.e. $\sigma < 0.3$, both $k^{\text{disp}}_{1\%}$ and $k^{\text{diff}}_{1\%}$ are similar for the RK3 and RK4 schemes. Regarding $k^{\text{diff}}_{1\%}$, the cut-off wavenumber monotonically decreases as σ increases, being this reduction higher for the RK4 scheme. On the other hand, the cut-off wavenumber $k^{\text{disp}}_{1\%}$ also decreases as σ is increased for the RK4 scheme, however, it does not show a clear tendency for the RK3 scheme.

The order of the scheme and the CFL numbers can be varied and combined to provide a similar cut-off wavenumber. The resulting computational cost varies considerable with these combinations, and is analysed here. Figure 7 shows the cut-off wavenumbers with respect to CPU time for the selected schemes. For instance, it is observed that $k^{\text{diff}}_{1\%}$ for UWC5-RK3 and UWC5-RK4 with $\sigma = 0.3$, and $k^{\text{diff}}_{1\%}$ for UWC7-RK4 with $\sigma = 0.9$, provide similar results. In terms of computational efficiency, the CPU time of UWC7-RK4 is much smaller than those of UWC5-RK3 and UWC5-RK4, thus being the former more efficient. Generally speaking, this analysis suggests that, for the same accuracy, is more efficient to use high order spatial schemes with low temporal order, and with a

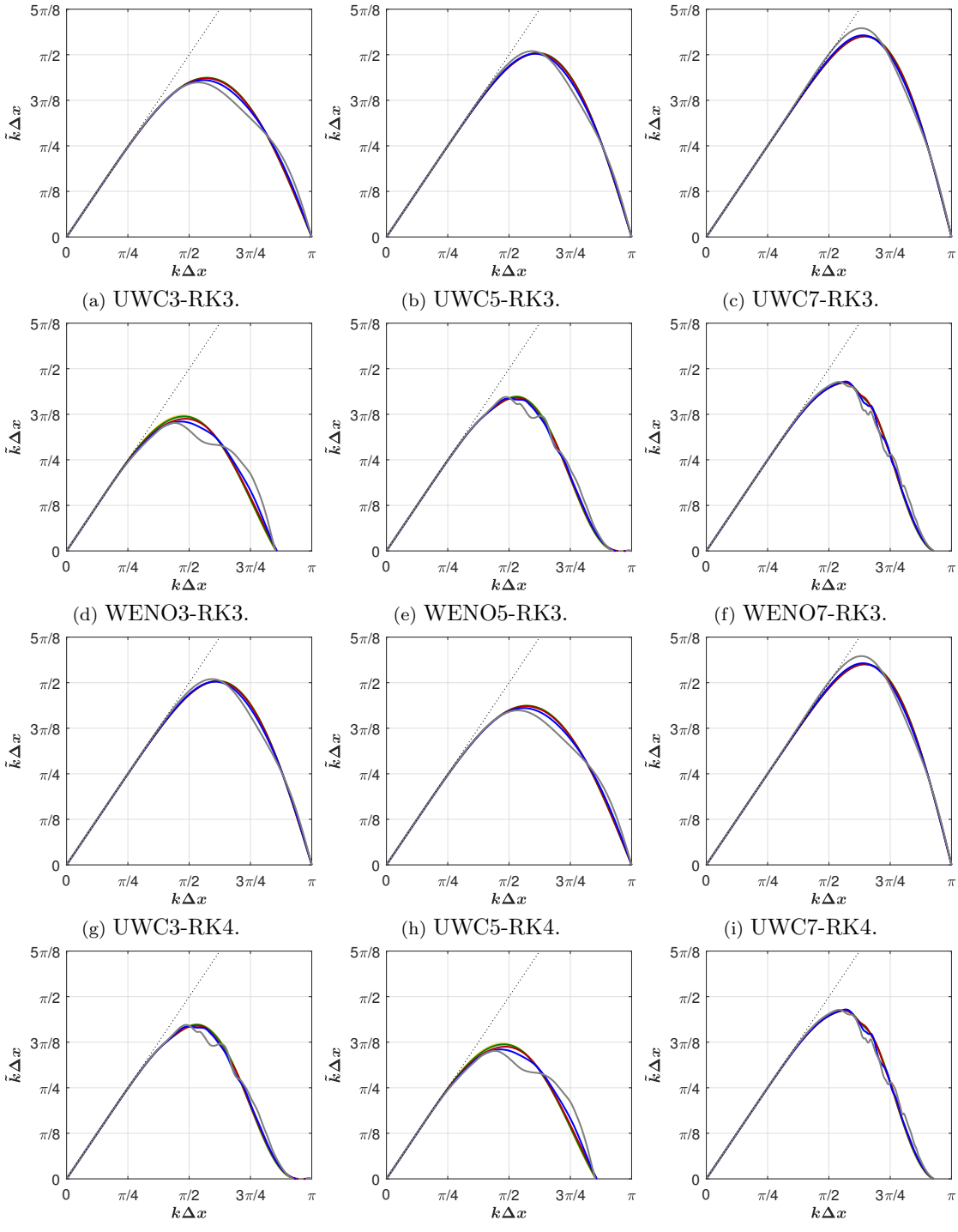

(a) UWC3-RK3. (b) UWC5-RK3. (c) UWC7-RK3.

(d) WENO3-RK3. (e) WENO5-RK3. (f) WENO7-RK3.

(g) UWC3-RK4. (h) UWC5-RK4. (i) UWC7-RK4.

(j) WENO3-RK4. (k) WENO5-RK4. (l) WENO7-RK4.

Figure 4: Approximate dispersion relation. CFL values: $\sigma = 0.001$ (—), $\sigma = 0.1$ (—), $\sigma = 0.3$ (—), $\sigma = 0.5$ (—) and $\sigma = 0.7$ (—). Ideal disperion relation (·····).

small CFL number.

Figure 8 shows both diffusion and dispersion relative errors associated to $k_{1\%}^{\text{disp}}$ and $k_{1\%}^{\text{diff}}$, respectively, and their variation with CFL number for all the numerical schemes.

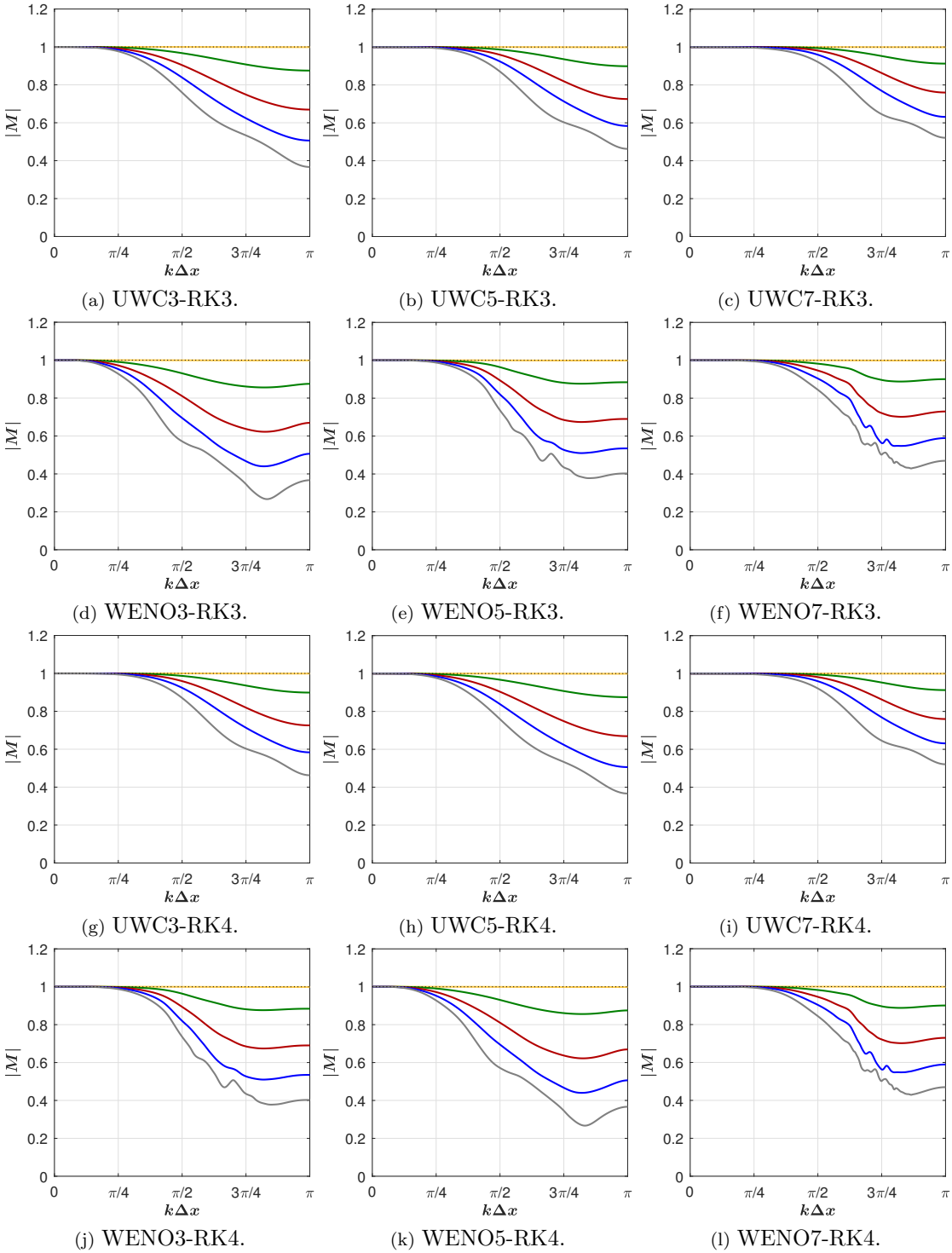

(a) UWC3-RK3. (b) UWC5-RK3. (c) UWC7-RK3.

(d) WENO3-RK3. (e) WENO5-RK3. (f) WENO7-RK3.

(g) UWC3-RK4. (h) UWC5-RK4. (i) UWC7-RK4.

(j) WENO3-RK4. (k) WENO5-RK4. (l) WENO7-RK4.

Figure 5: Approximate diffusion. CFL values: $\sigma = 0.001$ (—), $\sigma = 0.1$ (—), $\sigma = 0.3$ (—), $\sigma = 0.5$ (—) and $\sigma = 0.7$ (—). Ideal diffusion relation (····).

From these results, we observe that $\varepsilon_{1\%}^{\text{diff}}$ tends to increase for all schemes as σ increases. Additionally, $\varepsilon_{1\%}^{\text{disp}}$ decreases when σ increases, as observed in Figures 8b and 8d. This behaviour is explained by the high sensitivity of the diffusion relation to σ, which makes

Scheme	σ	$(k\Delta x)^{\text{disp}}_{1\%}$	$\varepsilon^{\text{diff}}_{1\%}$ (%)	$(k\Delta x)^{\text{diff}}_{1\%}$	$\varepsilon^{\text{disp}}_{1\%}$ (%)
FOU	0.1	0.29	0.37	0.46	0.03
	0.3	0.46	0.94	0.31	0.38
	0.5	0.98	0.00	0.28	0.45
	0.7	0.70	2.11	0.31	0.38
	0.9	0.87	3.22	0.48	0.03
UWC3-RK3	0.1	0.75	2.95	1.06	2.97
	0.3	0.75	2.95	0.81	0.90
	0.5	0.75	3.05	0.70	0.59
	0.7	0.78	3.49	0.63	0.47
	0.9	0.87	5.24	0.57	0.42
UWC5-RK3	0.1	1.09	4.81	1.41	1.25
	0.3	1.09	4.89	1.16	1.68
	0.5	1.14	5.72	1.02	1.20
	0.7	1.30	9.84	0.89	0.72
	0.9	0.93	2.25	0.76	0.33
UWC7-RK3	0.1	1.33	6.75	1.63	6.26
	0.3	1.34	6.96	1.40	5.30
	0.5	1.43	8.94	1.21	3.42
	0.7	1.21	4.46	1.00	1.67
	0.9	0.85	1.19	0.81	0.64
WENO3-RK3	0.1	0.79	11.47	0.78	2.97
	0.3	0.62	4.75	0.58	0.08
	0.5	0.62	4.75	0.50	0.20
	0.7	0.62	4.75	0.45	0.20
	0.9	0.62	4.75	0.41	0.15
WENO5-RK3	0.1	0.85	2.92	1.15	4.75
	0.3	0.85	2.95	0.94	0.80
	0.5	0.86	3.11	0.83	0.24
	0.7	0.90	3.69	0.75	0.12
	0.9	0.98	5.30	0.67	0.13
WENO7-RK3	0.1	1.04	4.43	1.31	1.08
	0.3	1.04	4.34	1.11	0.85
	0.5	1.06	4.77	0.99	0.84
	0.7	1.15	6.98	0.88	0.64
	0.9	1.01	3.56	0.77	0.36

Table 2: Non-dimensional wavenumbers and relative errors associated to the 1% rule, for FOU, UWC-RK3 and WENO-RK3 schemes.

$(k\Delta x)^{\text{diff}}_{1\%}$ to rapidly decrease as σ increases, whereas $(k\Delta x)^{\text{disp}}_{1\%}$ does not exhibit such behaviour.

The fact that with high CFL numbers the diffusion errors dominate over their dispersion counterpart may be beneficial for iLES simulations, as it implies that the poorly resolved waves are damped.

In Appendix B, the method of Pirozzoli has been applied to obtain the approximate dispersion-diffusion characteristics of different 2D WENO reconstruction schemes. The impact of the grid resolution has been studied alligning the wave direction with the diagonal direction of the grid ($k_x = k_y$). For this configuration, the results show that the differences between those schemes and their one dimensional counterparts are minor.

4.2. Numerical errors for Burgers' turbulence

In this section, the previous findings on the numerical performance of UWC and WENO schemes are challenged with one-dimensional Burgers' turbulence simulations [7, 10, 41]. According to [12], we augment the inviscid Burgers' equation (1 with the

Scheme	σ	$(k\Delta x)^{\text{disp}}_{1\%}$	$\varepsilon^{\text{diff}}_{1\%}$ (%)	$(k\Delta x)^{\text{diff}}_{1\%}$	$\varepsilon^{\text{disp}}_{1\%}$ (%)
UWC3-RK4	0.1	0.75	0.24	1.06	4.40
	0.3	0.75	0.73	0.81	1.57
	0.5	0.74	1.21	0.71	1.04
	0.7	0.74	1.65	0.65	0.84
	0.9	0.73	2.04	0.61	0.74
UWC5-RK4	0.1	1.09	0.22	1.41	4.99
	0.3	1.09	0.65	1.18	1.69
	0.5	1.08	1.06	1.07	1.09
	0.7	1.07	1.39	1.01	0.88
	0.9	1.03	1.59	0.95	0.81
UWC7-RK4	0.1	1.32	0.20	1.63	5.52
	0.3	1.32	0.60	1.42	1.82
	0.5	1.31	0.95	1.32	1.17
	0.7	1.28	1.21	1.25	0.96
	0.9	1.22	1.39	1.16	0.89
WENO3-RK4	0.1	0.79	0.98	0.78	1.07
	0.3	0.62	1.20	0.58	0.04
	0.5	0.62	2.07	0.50	0.02
	0.7	0.62	3.02	0.45	0.01
	0.9	0.62	4.03	0.42	0.01
WENO5-RK4	0.1	0.85	0.20	1.15	6.09
	0.3	0.85	0.59	0.94	1.87
	0.5	0.84	0.96	0.85	1.22
	0.7	0.84	1.32	0.80	0.96
	0.9	0.83	1.62	0.75	0.83
WENO7-RK4	0.1	1.04	0.21	1.31	5.33
	0.3	1.03	0.61	1.11	1.81
	0.5	1.02	0.96	1.03	1.19
	0.7	1.01	1.27	0.98	0.95
	0.9	0.98	1.48	0.93	0.8

Table 3: Non-dimensional wavenumbers and relative errors associated to the 1% rule, for various numerical schemes.

flux $f(u) = u^2/2$) with a white-in-time random force, $S(x,t)$. We follow [12, 38, 41] and compute the source term as

$$S(x,t) = \frac{A}{\sqrt{\Delta t}} \sum_{n=1}^{N_c} \frac{Z_n(t)}{\sqrt{\pi n}} \cos\left(\frac{2\pi n}{L} x\right), \tag{24}$$

where A is the amplitude of the fluctuations, for which we have adopted the value $A = 0.04$ proposed by Manzanero in [36]. This source term results from the sum of N_c harmonic modes, whose amplitude, $Z_n(t)/\sqrt{\pi n}$, includes a standard normal distribution $Z_n(t)$.

In absence of the forcing source term, fluctuations under the action of the convective term, $u\frac{\partial u}{\partial x}$, would evolve in time to form a set of large shock waves, reducing the initial randomness and minimizing turbulence. On the one hand, the energy spectrum associated to the energy transfer of these fluctuations is $E(k) \sim k^{-2}$ [10]. On the other hand, the energy transfer in the modes affected by $S(x,t)$ is more representative of the Navier-Stokes turbulence [29, 45], $E(k) \sim k^{-5/3}$.

Therefore, the solutions will present an energy spectrum divided in two regions. For small wavenumbers (i.e. the excitation region), the slope of the energy transference in the excitation region is $-5/3$. For large wavenumbers (also called inertial region), the

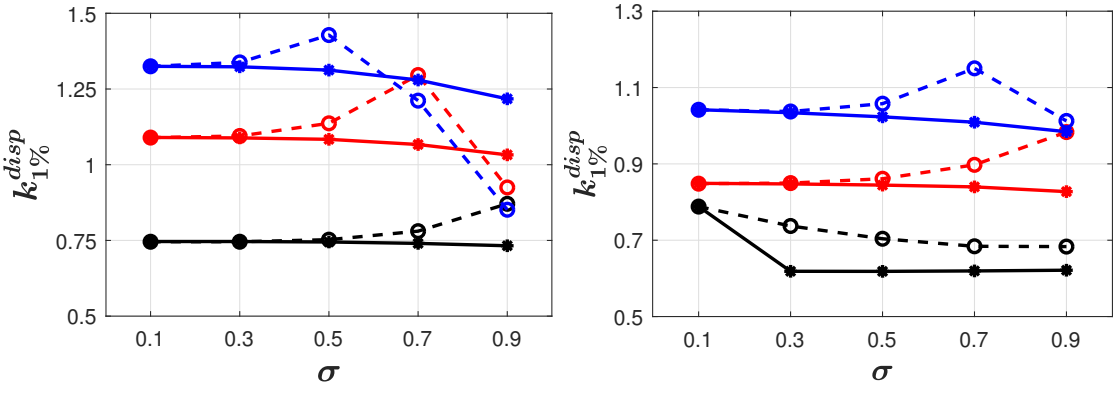

(a) UWC-RK. $k_{1\%}^{\text{disp}}$.

(b) WENO-RK. $k_{1\%}^{\text{disp}}$.

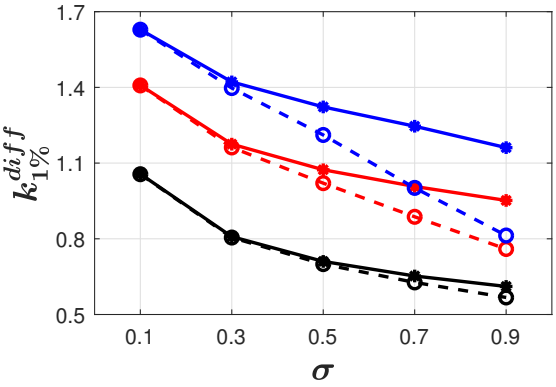

(c) UWC-RK. $k_{1\%}^{\text{diff}}$.

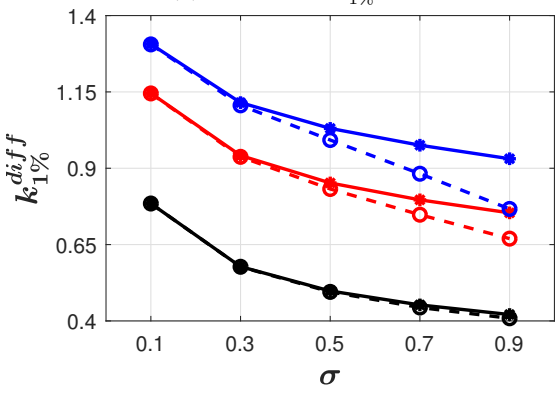

(d) WENO-RK. $k_{1\%}^{\text{diff}}$.

Figure 6: 1% rule for UWC and WENO schemes (third order (—◯—), fifth order (—◯—) and seventh order (—◯—)), with RK3 (dashed lines) and RK4, with $\sigma = 0.1$, $\sigma = 0.3$, $\sigma = 0.5$, $\sigma = 0.7$ and $\sigma = 0.9$. Fixed data: $N_c = 80$ - $N = 8192$.

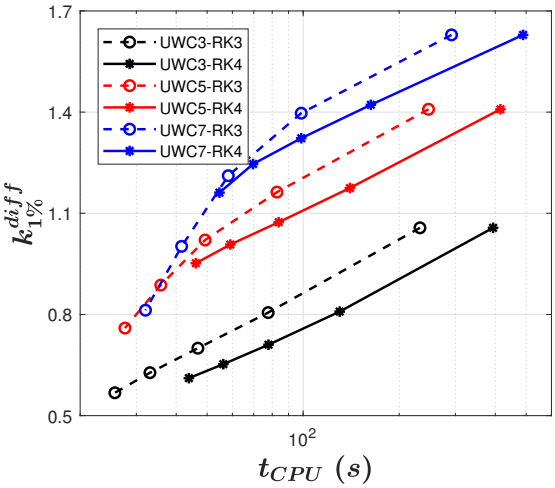

(a) CPU times vs. $k_{1\%}^{\text{diff}}$ for UWC schemes.

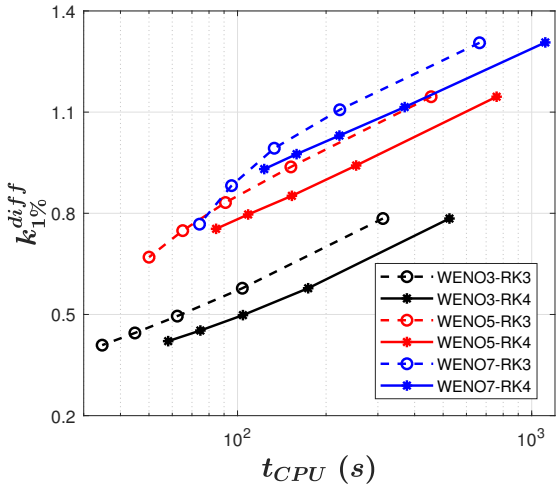

(b) CPU times vs. $k_{1\%}^{\text{diff}}$ for WENO schemes.

Figure 7: CPU times vs. $k_{1\%}^{\text{diff}}$. CFL numbers, $\sigma = 0.1$, 0.3, 0.5, 0.7 and 0.9, are displayed in decreasing order from left to right.

ratio of energy transference is -2. The switch from one behavior to the other depends on

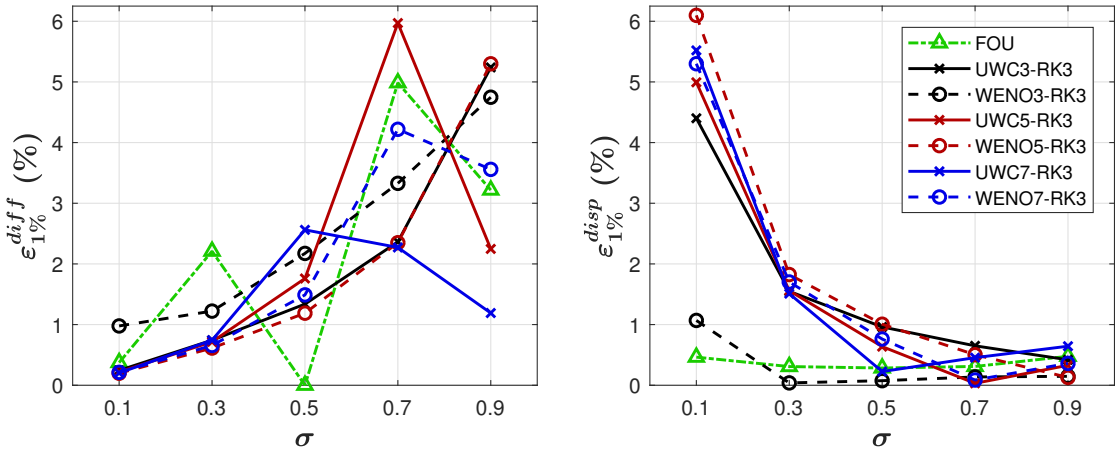

(a) Diffusion relative error, RK3 schemes.

(b) Dispersion relative error, RK3 schemes.

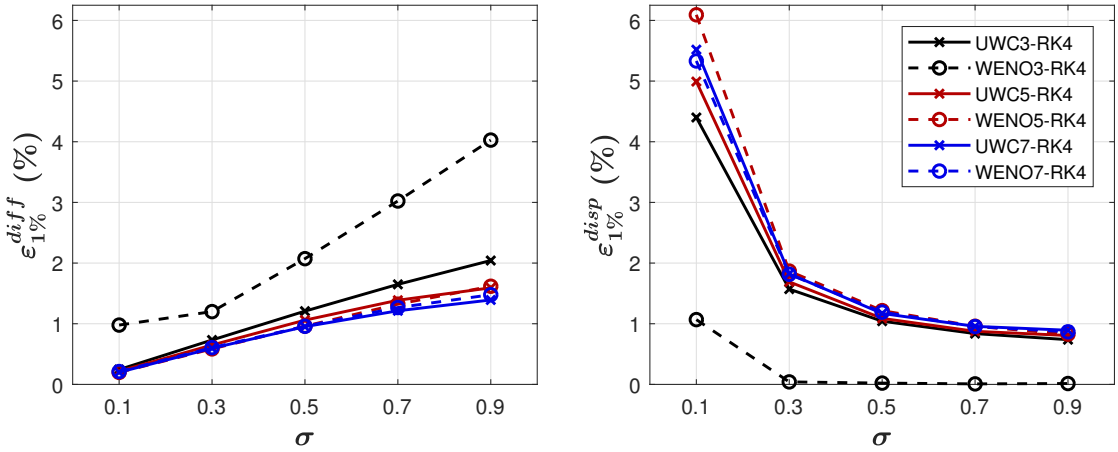

(c) Diffusion relative error, RK4 schemes.

(d) Dispersion relative error, RK4 schemes.

Figure 8: Evolution of the diffusion-dispersion relative error against the CFL.

the maximum number of exciting modes, N_c. Additionally, the behavior of the solution in the inertial region is independent of the number of initial modes, as shown in following sections.

In what follows, we solve Burgers' equation (1) with the source term (24), in the domain $\Omega = [-1, 1]$, with the initial condition $u(x, 0) = 1$ and with periodic boundary conditions. The final time is $t_F = 600$. As a result of the low amplitude of the source term, $A = 0.04$, the solution remains positive, and its average close to $u = 1$.

We first investigate the solution of Burgers' turbulence with the FOU, UWC and WENO schemes, up to 7-*th* order of accuracy. Because of the under–resolved nature of the problem, the choice of the numerical scheme (i.e. FOU, UWC or WENO) and the order of accuracy will have a noticeable impact in the numerical solution.

To illustrate the characteristics of the solution and the influence of the order of accuracy, the WENO3-RK3 and WENO5-RK3 schemes have been used to compute the solution at $t = 600$. The rest of the parameters are $\Delta t = 10^{-4}$, $N = 4096$, $N_c = 80$ and $\sigma = 0.9$. A comparison of the results are presented in Figure 9, showing that the solution final snapshot is similar for both schemes except for the smaller scales in the WENO5-RK3 solution, as a result of its higher accuracy (see Figures 9a–9d).

Prior to the analysis of the performance of the schemes, it is necessary to study

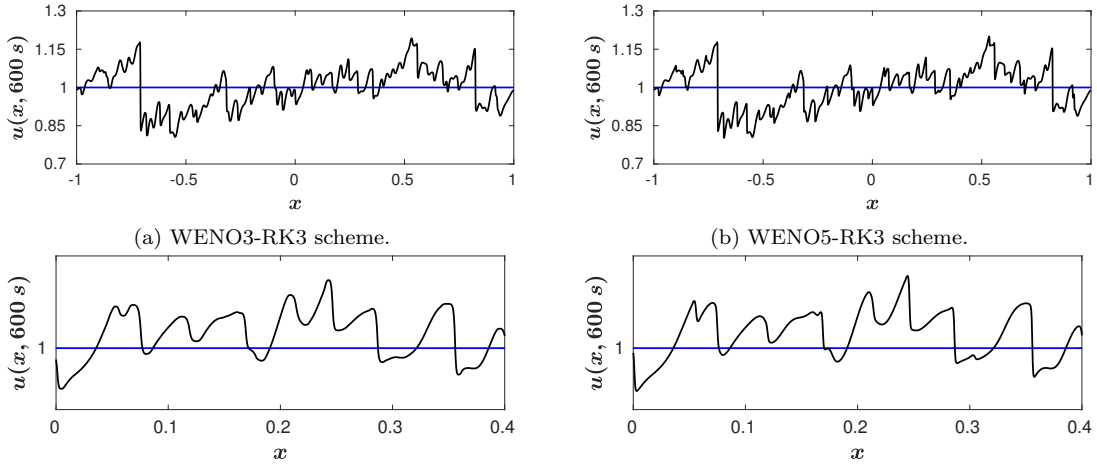

(a) WENO3-RK3 scheme.

(b) WENO5-RK3 scheme.

(c) WENO3-RK3 scheme (zoom).

(d) WENO5-RK3 scheme (zoom).

Figure 9: Solution computed using the WENO3-RK3 and WENO5-RK3 schemes at $t = 600$, setting $\Delta t = 0.0001$, $N_c = 80$ and $N = 8192$.

the sensitivity of the numerical solution to some relevant parameters of the problem, such as the maximum number of excitation modes, N_c and the number of cells, N. Figure 10 shows the computed energy cascade provided by the WENO5-RK3 scheme in three different grids, with $N = 4096$, $N = 8192$ and $N = 16384$ cells. Note we have represented the compensated spectrum, $E(k)/k^{-2}$. The excitation and the inertial range are delimited by N_c, which has been kept constant in this test. The "1% rule" wavenumbers, $k_{1\%}^{\text{disp}}$ and $k_{1\%}^{\text{diff}}$ are also displayed. Such values are transformed from their non-dimensional counterparts presented in Table 2, $(k\Delta x)_{1\%}^{\text{disp}}$ and $(k\Delta x)_{1\%}^{\text{diff}}$, following

$$k_{1\%} = \frac{N}{2\pi}(k\Delta x)_{1\%}. \tag{25}$$

The results in Figure 10 evidence that wavenumbers $k_{1\%}^{\text{disp}}$ and $k_{1\%}^{\text{diff}}$ scale properly with the mesh size. The green dashed/dotted lines represent the intersection points between the energy cascades with $k_{1\%}^{\text{disp}}$ and $k_{1\%}^{\text{diff}}$, revealing mesh independence.

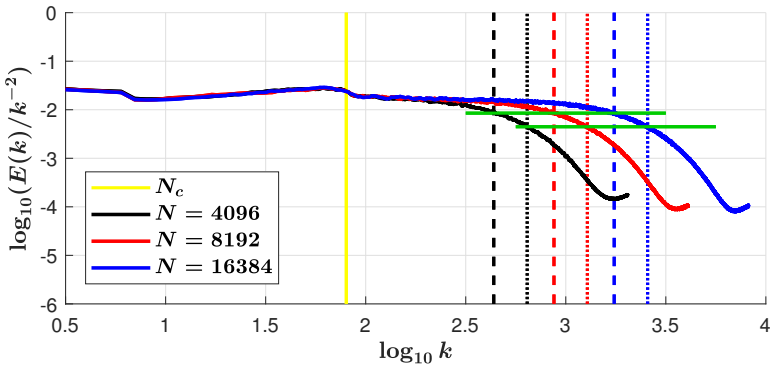

Figure 10: Superposition of energy cascades for WENO5 scheme with various cell numbers: $k_{1\%}^{\text{disp}}(N = 4096)$ (▪▪▪), $k_{1\%}^{\text{diff}}(N = 4096)$ (▬ ▬), $k_{1\%}^{\text{disp}}(N = 8192)$ (▪▪▪), $k_{1\%}^{\text{diff}}(N = 8192)$ (▬ ▬), $k_{1\%}^{\text{disp}}(N = 16384)$ (▪▪▪) and $k_{1\%}^{\text{diff}}(N = 16384)$ (▬ ▬).

We now perform a complete analysis of the proposed schemes, namely the FOU, UWC3-RK3, UWC5-RK3, UWC7-RK3, WENO3-RK3, WENO5-RK3 and WENO7-RK3, using four different CFL numbers: $\sigma = 0.1$, $\sigma = 0.3$, $\sigma = 0.5$ and $\sigma = 0.9$.

4.2.1. FOU scheme

The results for the FOU scheme are included in Figure 11. As expected, it is observed that the FOU scheme introduces a high numerical diffusion from medium to large wavenumbers. The diffusion decreases as σ gets closer to 1 (as seen previously in Figure 8), and consequently the numerical cascade is not able to capture the theoretical slope even in a small extent of the wavenumber range.

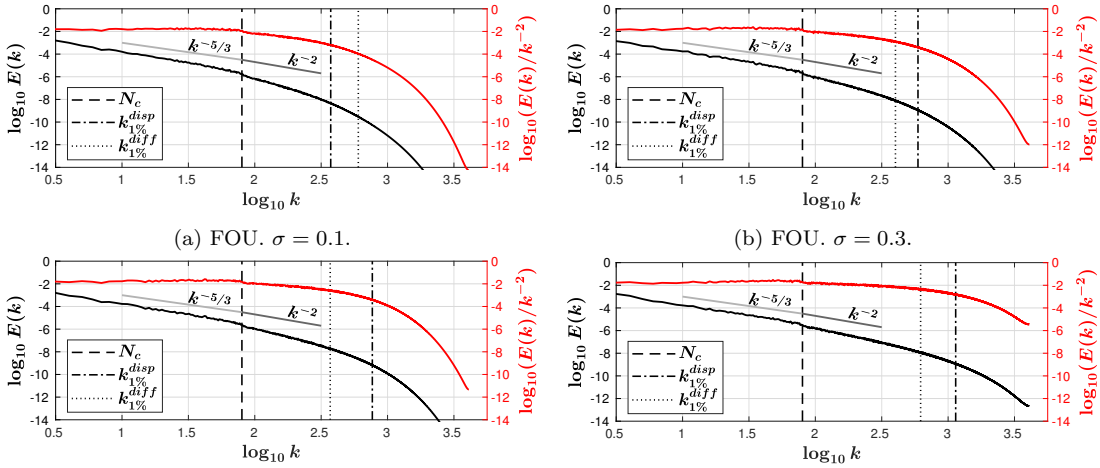

(a) FOU. $\sigma = 0.1$.

(b) FOU. $\sigma = 0.3$.

(c) FOU. $\sigma = 0.5$.

(d) FOU. $\sigma = 0.9$.

Figure 11: Energy cascades for FOU scheme, with $\sigma = 0.1$, $\sigma = 0.3$, $\sigma = 0.5$ and $\sigma = 0.9$. Fixed data: $N_c = 80$ - $N = 8192$.

4.2.2. UWC schemes

UWC schemes are capable to capture the theoretical slope on a wide range of wavenumbers in the inertial region as shown in Figure 12. The energy cascades are characterized by an energy pile-up at high wavenumbers where the energy increases locally before it is entirely dissipated [40]. The magnitude of this energy pile-up increases with the order of the scheme and the "1% rule" accurately predicts the location of the maximum energy pile-up in the energy cascade. The cut-off wavenumber $k_{1\%}^{\text{diff}}$ approaches the wavenumber at which the maximum is located. Moreover, we locate the transition zone between the inertial and the diffusion region, as hypothesized. This result is evidenced in Figure 13, where $k_{1\%}^{\text{disp}}$ and $k_{1\%}^{\text{diff}}$ values are represented alongside the wavenumber associated to the maximum pile-up.

The UWC5-RK3 and UWC7-RK3 schemes present a high coincidence between the position of maximum pile-up and the "1% rule" wavenumbers. The UWC3-RK3 shows the greatest disagreement, as it introduces higher numerical diffusion and the diffusion error prevails over the dispersion error. Even though $k_{1\%}^{\text{disp}}$ and $k_{1\%}^{\text{diff}}$ are both good indicators of the location of the maximum pile-up, a sharper agreement is observed for $k_{1\%}^{\text{disp}}$, which is the one chosen in [41].

The comparison of the results in Figures 12a, 12c and 12e (3-rd order, 5-th order and 7-th order) shows that the value of the compensated spectrum in $k_{1\%}^{\text{disp}}$ and $k_{1\%}^{\text{diff}}$ for

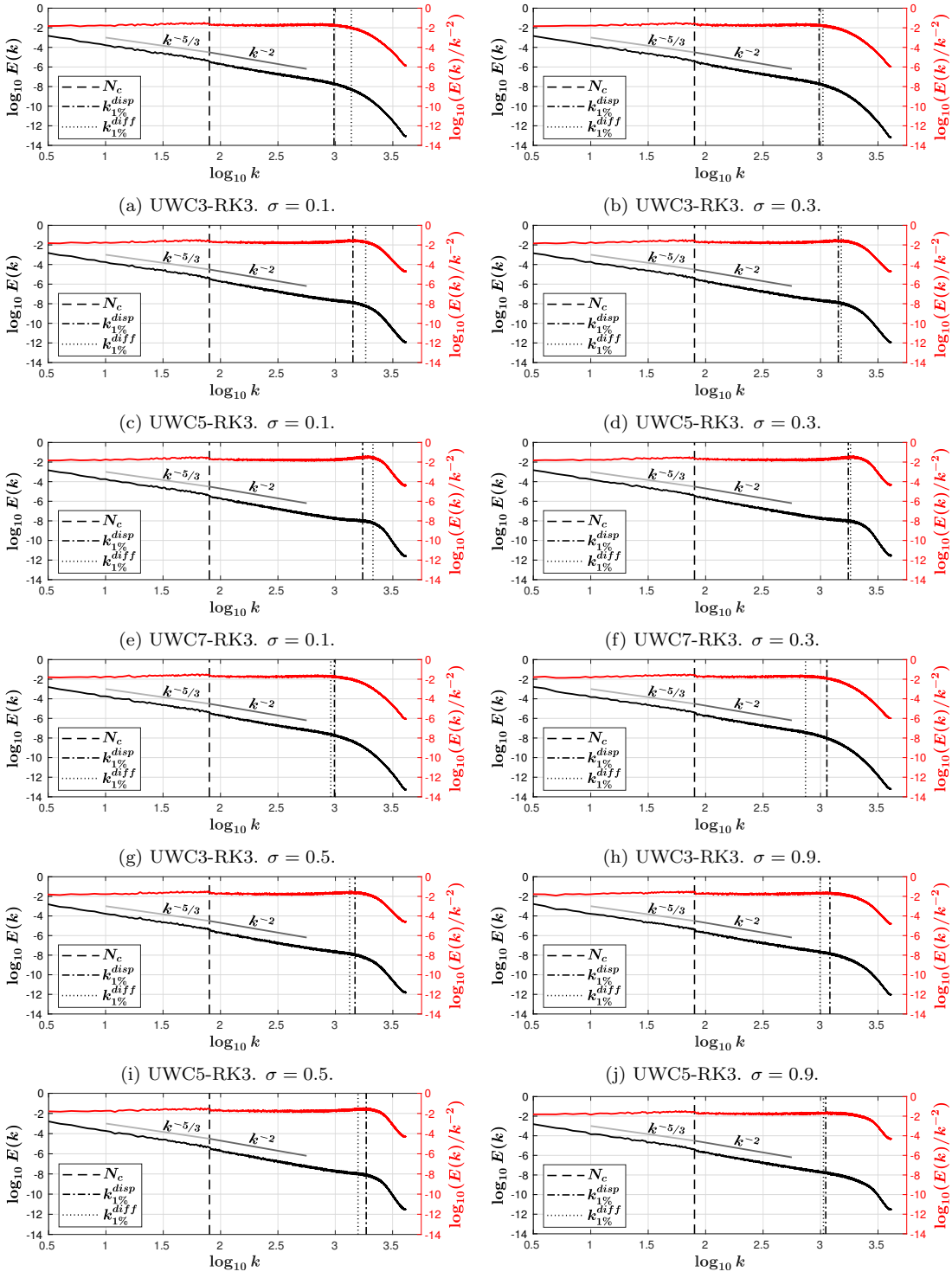

(a) UWC3-RK3. $\sigma = 0.1$.

(b) UWC3-RK3. $\sigma = 0.3$.

(c) UWC5-RK3. $\sigma = 0.1$.

(d) UWC5-RK3. $\sigma = 0.3$.

(e) UWC7-RK3. $\sigma = 0.1$.

(f) UWC7-RK3. $\sigma = 0.3$.

(g) UWC3-RK3. $\sigma = 0.5$.

(h) UWC3-RK3. $\sigma = 0.9$.

(i) UWC5-RK3. $\sigma = 0.5$.

(j) UWC5-RK3. $\sigma = 0.9$.

(k) UWC7-RK3. $\sigma = 0.5$.

(l) UWC7-RK3. $\sigma = 0.9$.

Figure 12: Energy cascades for UWC schemes, with $\sigma = 0.1$, $\sigma = 0.3$, $\sigma = 0.5$ and $\sigma = 0.9$. Fixed data: $N_c = 80$ - $N = 8192$.

the UWC3-RK3 scheme lies beneath the ideal trend. On the other hand, these values of the compensated spectrum lie over the ideal trend for the UWC5-RK3 and UWC7-RK3

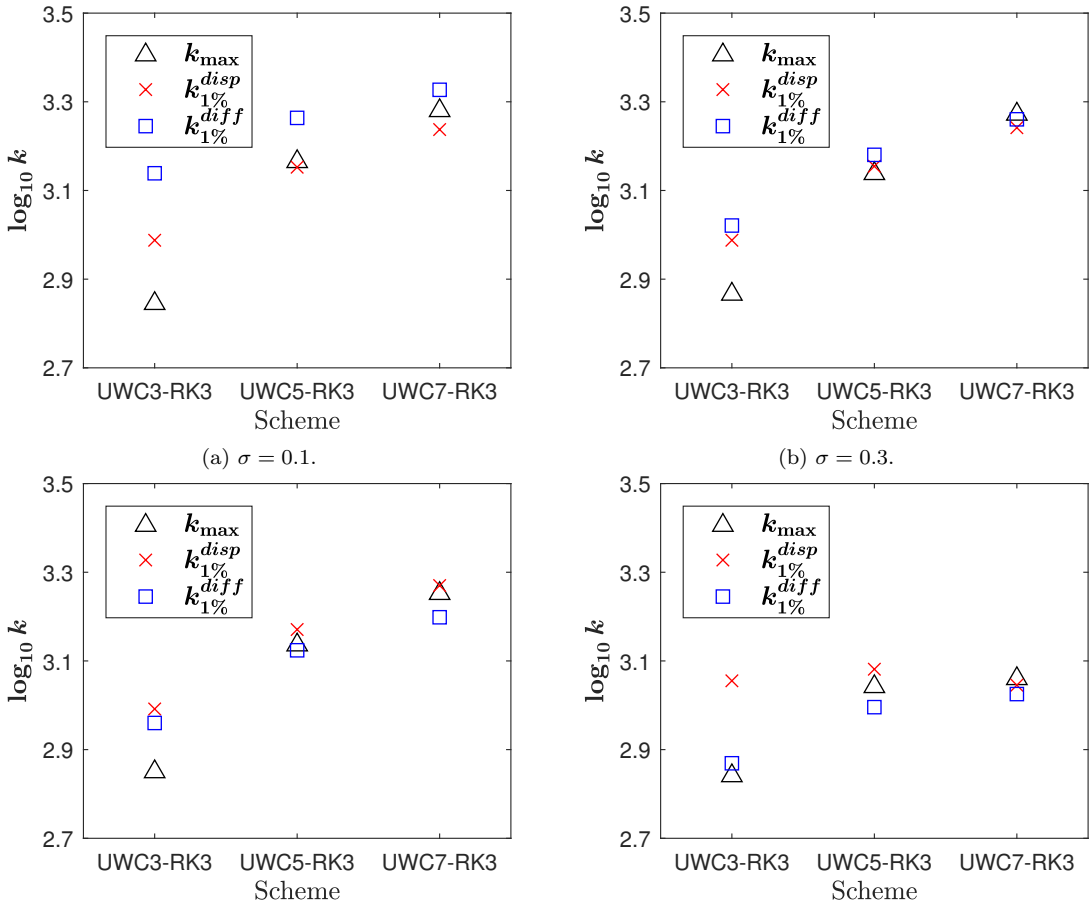

(a) $\sigma = 0.1$.

(b) $\sigma = 0.3$.

(c) $\sigma = 0.5$.

(d) $\sigma = 0.9$.

Figure 13: Assessment of the coincidence of $k_{1\%}^{\text{disp}}$ and $k_{1\%}^{\text{diff}}$ with the positions of the pile-up maximum for UWC-RK3 schemes. Fixed data: $N_c = 80$ - $N = 8192$.

schemes, due to the energy pile-up.

We propose a simple criterion (detailed in Appendix C) to detect the magnitude of the deviation of the computed energy spectrum at the wavenumbers given by the "1% rule" with respect to the extrapolated inertial range. We define the energy deviation, Λ, such that a positive energy deviation indicates the presence of an energy pile–up, and negative otherwise. In Figure 14 we have represented the results of the energy deviation criterion, computed by (C.1) using $k_{1\%}^{\text{disp}}$ and $k_{1\%}^{\text{diff}}$, for the UWC-RK3 schemes with $\sigma = 0.1$, $\sigma = 0.3$, $\sigma = 0.5$ and $\sigma = 0.9$. The figure evidences that the energy pile-up increases as the order is increased and that the UWC3-RK3 does not exhibit such pile-up, as stated before. Moreover, the energy pile-up decreases as σ increases. This behaviour is related to the raise of the diffusion error measured for $k_{1\%}^{\text{disp}}$, also shown in Figure 14. Furthermore, the figure also shows that energy deviations measured by $\Lambda^{\text{diff}} < 0$ show a lower dependency on the order of accuracy as the CFL number increases (see Figure 14d).

Regarding the application of UWC to iLES simulation, it must be noted that low values of σ would involve a very high dispersion error due to the energy pile-up. As σ increases the dispersion error at $k_{1\%}^{\text{diff}}$ notably reduced, allowing to follow closely the theoretical energy cascade, and making these schemes more suitable in for iLES. A high

diffusion error for $k > k_{1\%}^{\text{disp}}$ implies the diffusion of turbulent fluctuations that would not be properly propagated by the numerical scheme. These fluctuations will be attenuated by the UWC schemes when using high CFL numbers, avoiding possible dispersion errors and energy pile-up. In this case, the numerical scheme would play the role of a subgrid model, implicitly filtering the small scales.

To complete this analysis, the most relevant results obtained with UWC-RK4 schemes have been included in Appendix D. Firstly, with regard to energy cascades, noticeable differences are only observed for high CFL numbers, such as 0.5 and as 0.9, shown in Figure D.25. Those CFL numbers feature an energy pile-up, contrarily when using UWC-RK3 scheme. Secondly, as with RK3 schemes, Figure D.26 shows that the cut-off wavenumber $k_{1\%}^{\text{diff}}$ locates the transition zone between the inertial and the dissipation region. It approximates the wavenumber at which the maximum pile-up is located. Thirdly, Figure D.27 shows a similar trend as UWC-RK3 schemes. In conclusion, UWC-RK4 schemes exhibit a similar behavior to UWC-RK3 schemes, with some small differences at high CFL numbers where the former are less dissipative.

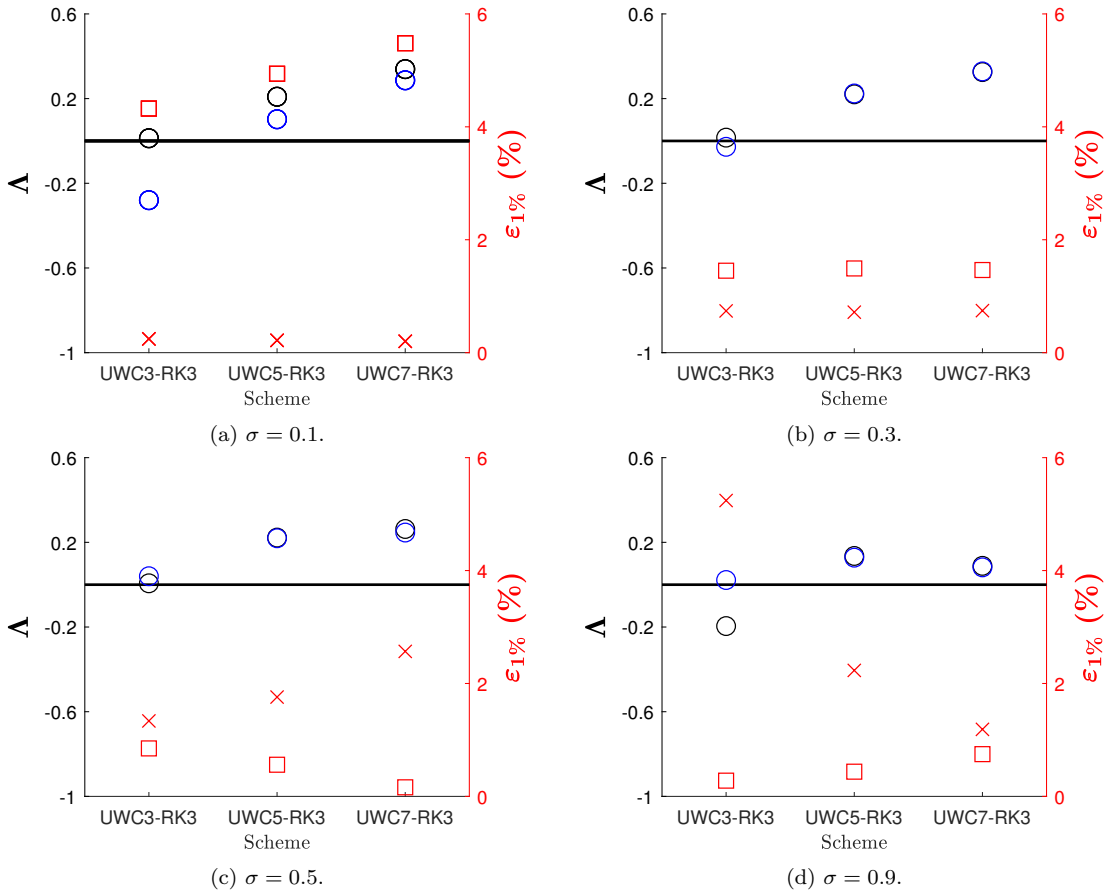

(a) $\sigma = 0.1$.

(b) $\sigma = 0.3$.

(c) $\sigma = 0.5$.

(d) $\sigma = 0.9$.

Figure 14: Energy pile-up criterion for UWC-RK3 schemes, with $\sigma = 0.1$, $\sigma = 0.3$, $\sigma = 0.5$ and $\sigma = 0.9$. Contents: (—) $\Lambda = 0$, ◯ Λ^{disp}, ◯ Λ^{diff}, □ Dispersion error (%) y × Diffusion error (%). Fixed data: $N_c = 80$ - $N = 8192$.

4.2.3. WENO schemes

The energy cascades for WENO schemes are displayed in Figure 15. The main difference with respect to the previous results is the absence of the energy pile-up. This

is directly related to the high amount of numerical diffusion provided by the WENO schemes in comparison with the UWC schemes. This is evidenced in Figure 16, where the energy deviations, Λ, are negative in all cases. It is worth noting that the WENO7-RK3, having a higher order of accuracy than the UWC3-RK3, provides a slightly steeper spectrum in the inertial range due to the intrinsic diffusive properties of the WENO schemes. Such schemes use a dynamic stencil selection that reduces the order of accuracy to one at shocked regions, which explains this behavior.

Figure 16 shows that dispersion errors are reduced as σ increases, in the same way as for the UWC-RK schemes. This makes WENO-RK schemes highly robust for iLES, though their high diffusion errors could compromise their accuracy and their ability to capture small scales. An important observation inferred from Figure 16 is that the energy deviations measured by Λ^{diff} have a similar magnitude for WENO3-RK3, WENO5-RK3 and WENO7-RK3 schemes. In other words, the ratio between the energy of the numerical solution and that of the extrapolated trend in $k_{1\%}^{\text{diff}}$ is alike amongst all WENO-RK schemes, with independence of the order of accuracy, and for each choice of the CFL number σ (specially for $\sigma = 0.1$). This may be beneficial for numerical schemes using local time stepping or in flows where large disparity of scales co-exist (e.g. turbulent flows). On the other hand, the energy deviations measured at $k_{1\%}^{\text{disp}}$, Λ^{disp}, show larger variations amongst the WENO3-RK3, WENO5-RK3 and WENO7-RK3 schemes and no clear conclusions can be extracted. Finally, it is also observed that the level of energy of the mode associated to $k_{1\%}^{\text{diff}}$, $E(k_{1\%}^{\text{diff}})$, does not have a strong dependency on the order of accuracy.

With regard to the higher order integration in time, the results of WENO-RK4 schemes are very similar to those of WENO-RK3 schemes, so that the same conclusions can be drawn from them. In this case, differences are smaller than for UWC schemes, as time integration errors are usually smaller than those of the WENO reconstruction. For the sake of brevity, results for WENO-RK4 schemes are not displayed.

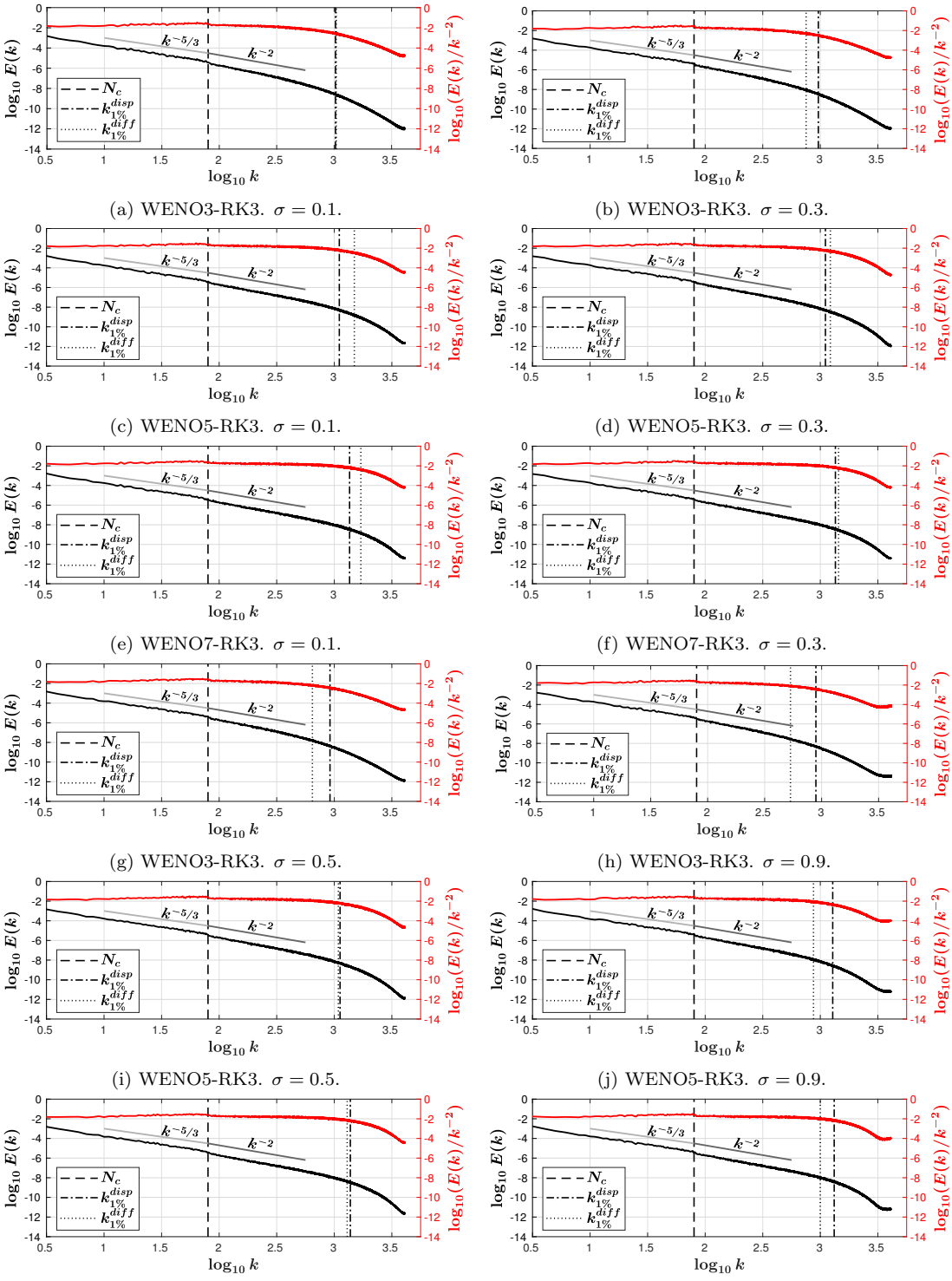

(a) WENO3-RK3. $\sigma = 0.1$.

(b) WENO3-RK3. $\sigma = 0.3$.

(c) WENO5-RK3. $\sigma = 0.1$.

(d) WENO5-RK3. $\sigma = 0.3$.

(e) WENO7-RK3. $\sigma = 0.1$.

(f) WENO7-RK3. $\sigma = 0.3$.

(g) WENO3-RK3. $\sigma = 0.5$.

(h) WENO3-RK3. $\sigma = 0.9$.

(i) WENO5-RK3. $\sigma = 0.5$.

(j) WENO5-RK3. $\sigma = 0.9$.

(k) WENO7-RK3. $\sigma = 0.5$.

(l) WENO7-RK3. $\sigma = 0.9$.

Figure 15: Energy cascades for WENO schemes, with $\sigma = 0.1$, $\sigma = 0.3$, $\sigma = 0.5$ and $\sigma = 0.9$. Fixed data: $N_c = 80$ - $N = 8192$.

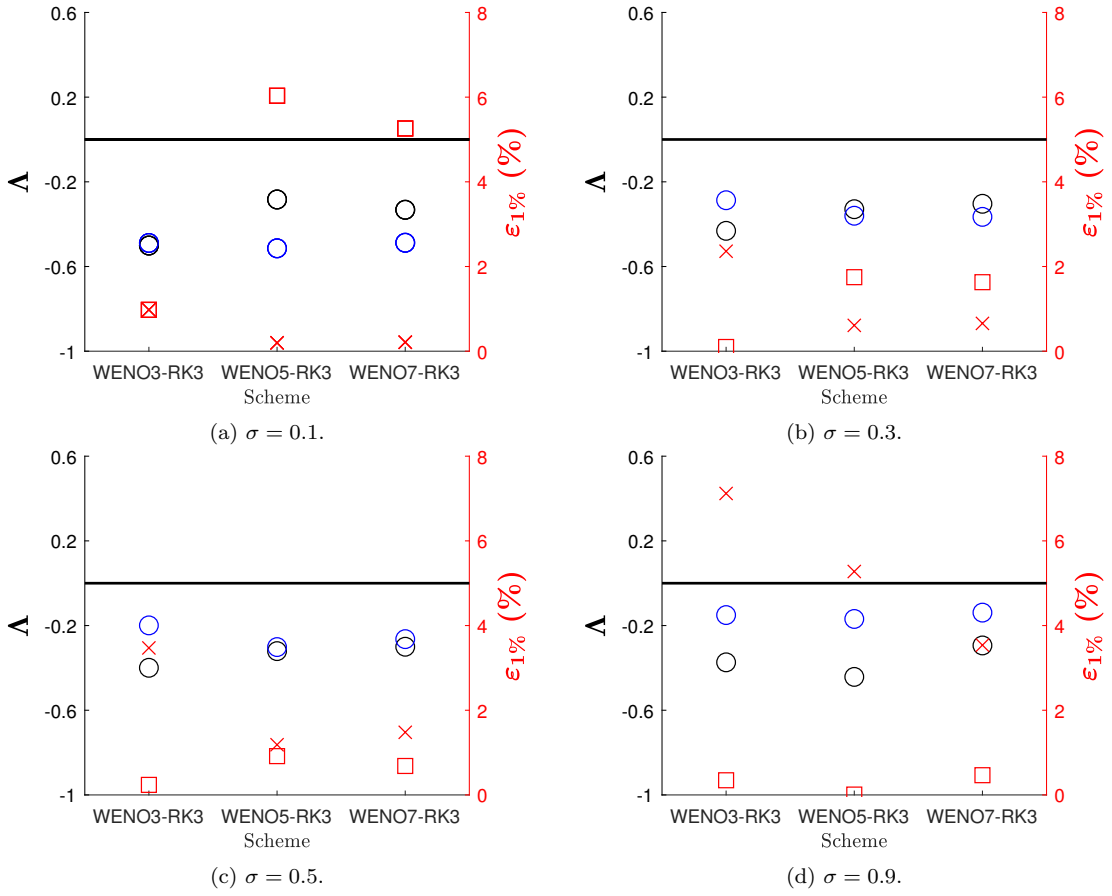

(a) $\sigma = 0.1$. (b) $\sigma = 0.3$.

(c) $\sigma = 0.5$. (d) $\sigma = 0.9$.

Figure 16: Energy pile-up criterion for WENO-RK3 schemes, with $\sigma = 0.1$, $\sigma = 0.3$, $\sigma = 0.5$ and $\sigma = 0.9$. Contents: (—) $\Lambda = 0$, ◯ Λ^{disp}, ◯ Λ^{diff}, □ Dispersion error (%) and × Diffusion error (%). Fixed data: $N_c = 80$ - $N = 8192$.

4.2.4. Comparisons between UWC and WENO schemes

We finally compare UWC-RK and WENO-RK schemes. Figure 17 shows a logarithmic plot of $E(k_{1\%}^{\text{diff}})$, for the 3-rd, 5-th and 7-th UWC-RK3 and WENO-RK3 schemes using $\sigma = 0.1,\ 0.3,\ 0.5$ and 0.9. A high similarity is observed between the 5-th and the 7-th order scheme (both UWC and WENO), whereas the 3-rd order scheme shows an increasing deviation from the 5-th and 7-th order schemes as the value of σ is increased. Regarding the dependency of $E(k_{1\%}^{\text{diff}})$ on σ, WENO schemes show a slightly higher sensitivity, whereas UWC schemes show very small variations as σ is increased. It must be noted that in the case of the 3-rd, 5-th and 7-th UWC-RK3 schemes with $\sigma = 0.1$, $E(k_{1\%}^{\text{diff}})$ is virtually the same for all of them. The particular case of the WENO schemes for $\sigma = 0.1$ is depicted in Figure 18.

In Figure 19, we analyze the validity of the "1% rule" to define a cut-off wavenumber from the approximate dispersion-diffusion relation that successfully translates to non-linear problems. Figure 19a represents the magnitude of $E(k_{1\%}^{\text{diff}})$ with respect to the cut-off error percentage for the 3-rd, 5-th and 7-th order WENO-RK3 schemes with $\sigma = 0.1$. It is observed that cut-off percentages lower or equal than 1% yield to a very similar energy magnitude, $E(k_{1\%}^{\text{diff}})$, in particular for the 5-th and 7-th order schemes. As the percentage is increased from 1% to 10%, strong differences appear among the energy

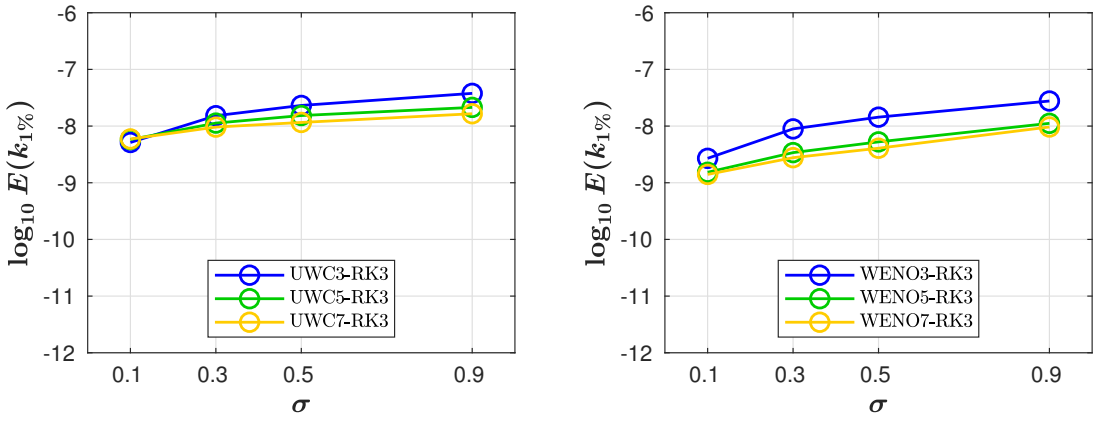

(a) UWC schemes.

(b) WENO schemes.

Figure 17: Evaluation of the computed energy at $k_{1\%}^{\text{diff}}$ as a function of σ. Fixed data: $N_c = 80$ - $N = 8192$.

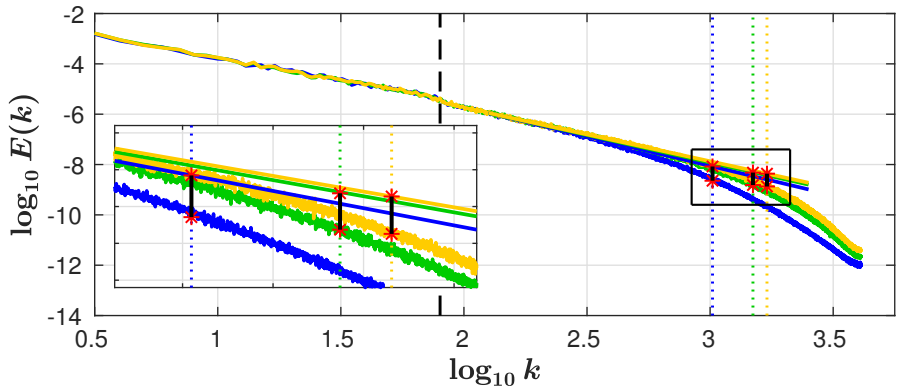

Figure 18: Detail of the energy cascade for (—) WENO3-RK3, (—) WENO5-RK3 and (—) WENO7-RK3 schemes showing their corresponding energy deviations, Λ^{diff} (black segments). Fixed data: $N_c = 80$ - $N = 8192$ - $\sigma = 0.1$.

magnitude predicted by the dispersion-diffusion relation associated to the percentages. The same behavior is noticed in Figure 19b, where Λ^{diff} is plotted against the cut-off error percentage. In this case, also the 3-rd order scheme matches very well the 5-th and 7-th order schemes. Therefore, we confirm the validity of the "1% rule" to show what percentages of deviation bigger than 1% would not be suitable.

5. Concluding remarks

In this work, we quantify the numerical errors of two widespread high-order finite volume reconstructions, the WENO and the UWC methods, in combination with 3-rd and 4-th order RK integrators. The approximate non-linear dispersion-diffusion analysis by Pirozzoli [44] has been used to estimate the fully-discrete errors in the schemes. Unlike most of previous work, the approximate dispersion-diffusion analysis has been applied to the space-time discrete equations and not only to the semi-discrete operators.

The "1% rule", introduced by Moura et al. [41] in the framework of DG schemes, has been considered to quantify numerical errors. A sensitivity analysis of the approximate

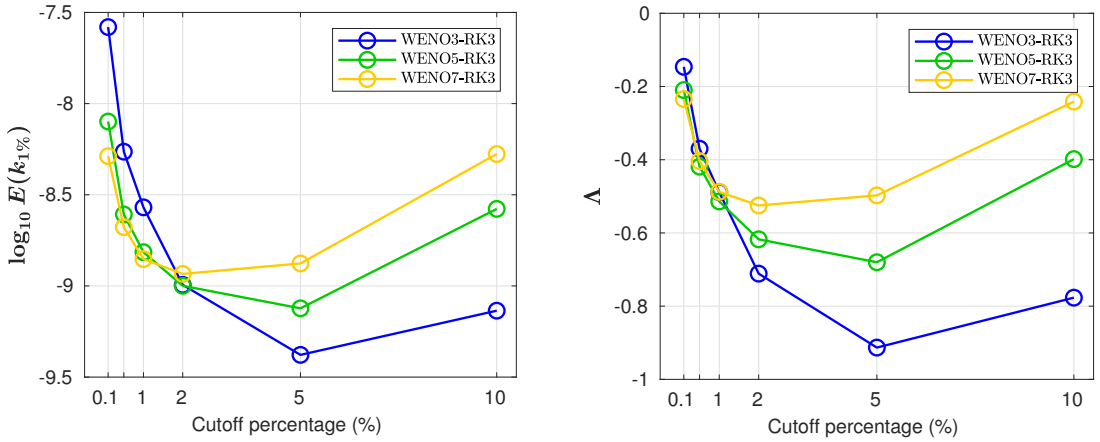

(a) $E(k_{1\%}^{\text{diff}})$ vs. cut-off percentage.

(b) Energy deviation vs. cut-off percentage.

Figure 19: Evaluation of the computed energy, $E(k_{1\%}^{\text{diff}})$, and the energy deviation, Λ^{diff}, as functions of the error percentage for WENO schemes. Fixed data: $N_c = 80$ - $N = 8192$ - $\sigma = 0.1$.

dispersion-diffusion relation to the grid size has been carried out to assess its suitability to obtain the wavenumbers and diffusion-dispersion errors associated to the "1% rule". A number of points greater than $N = 4000$ has proved to be required in order to obtain accurate results, in particular regarding the dispersion and diffusion errors at $k_{1\%}^{\text{diff}}$ and $k_{1\%}^{\text{disp}}$. The analyses for linear and non-linear problems provide guidelines for iLES simulations.

In general, WENO schemes involve a higher diffusion than their linear counterparts, i.e. UWC schemes. This is because they feature a dynamic stencil selection to fulfill the essentially non-oscillatory property that reduces the scheme to first order at discontinuities. The approximate dispersion-diffusion relation shows that they also involve a higher dispersion than the UWC schemes. The "1% rule" evidences that the cut-off wavenumbers, $k_{1\%}^{\text{diff}}$ and $k_{1\%}^{\text{disp}}$, are larger for UWC schemes than WENO schemes. Furthermore, both quantities increase as the order of accuracy of the scheme is increased. The dependency on the CFL number of such quantities has also been studied. On the one hand, $k_{1\%}^{\text{diff}}$ is reduced as σ increases for all the schemes, as the time-stepping RK3 and RK4 methods accumulate larger errors when increasing Δt. On the other hand, $k_{1\%}^{\text{disp}}$ does not show a clear trend for the RK3 schemes, but it does decrease as the CFL number is increased for the RK4 schemes.

The conclusions stated above agree with previous literature [22, 28, 33, 39, 40, 46, 57] and are evidenced when considering the application of the schemes to the Burgers' turbulence problem. The analysis of the intertial range of the energy spectrum of the numerical solution shows the presence of an energy pile-up at high wavenumbers for UWC-RK3 and UWC-RK4 schemes. This pile-up is reduced as the CFL number is increased in the case of UWC-RK3 schemes, and it remains for UWC-RK4 schemes. On the other hand, both WENO-RK3 and WENO-RK4 schemes exhibit a steeper spectrum in the inertial region due to the excessive diffusion at shocked regions.

In view of these results, both UWC-RK3 and UWC-RK4 schemes, and WENO-RK3 and WENO-RK4 schemes may be a suitable choice for iLES turbulence modelling, taking into account several considerations. UWC-RK3 and UWC-RK4 schemes will accurately reproduce a wider range of the energy spectrum than WENO schemes, though energy

pile-up may appear just before the diffusion region. Such pile-up is reduced as the CFL number increases for UWC-RK3 schemes, making those schemes better candidates in this situation. In this respect, Figure 14 shows that the pile-up virtually disappears and the dispersion error is strongly reduced as the CFL number increases.

It is worth noting that in presence of strong shocks (specially in 2D and 3D problems), UWC schemes may not be robust enough and may become unstable. On the other hand, WENO schemes offer a higher robustness even in presence of strong shocks, motivated by their essentially non-oscillatory property. This is done at the cost of involving a relatively high numerical diffusion, due to the dynamic stencil selection. Both the approximate dispersion-diffusion analysis and the results from Burgers' turbulence show that this amount of diffusion may prevent the scheme from recovering the k^{-2} slope in a large extent of the inertial region, specially the 3-rd and 4-th order WENO methods. WENO schemes are not sensitive to the CFL number, showing similar results for all the choices of this parameter. The conclusions obtained for UWC and WENO schemes with $\sigma = 0.1$ were previously reported for a decaying Burgers' turbulence problem in [40], where the authors only focused on the analysis of the semidiscrete operators.

The validity of the "1% rule" has been assessed for the 3-rd, 5-th and 7-th order WENO-RK3, WENO-RK4, UWC-RK3 and UWC-RK4 schemes. It has been confirmed that we can use the cut-off wavenumber $k_{1\%}^{\text{diff}}$ as a good estimator of the beginning of the diffusion region [41]. Two different criteria, based on the energy deviation from the extrapolated trend, Λ^{diff}, and the energy magnitude at $k_{1\%}^{\text{diff}}$, are used as a tool of analysis in combination with the "1% rule". Several observations for the schemes herein considered are pointed out:

(a) for UWC-RK3 and UWC-RK4 schemes, the "1% rule" accurately predicts the location of the maximum energy pile-up in the energy cascade. The cut-off wavenumber $k_{1\%}^{\text{disp}}$ approaches the wavenumber at which the maximum is located (see Figures 13 and D.26). Note that $k_{1\%}^{\text{diff}}$ is also a good estimator;

(b) different order WENO-RK3 and WENO-RK4 schemes provide a similar level of energy deviation with respect to the extrapolated trend, i.e. the quantity Λ^{diff} is alike among them (see Figures 16 and 19b). Additionally, Λ^{diff} for UWC schemes shows a high sensitivity with respect to the order of the scheme due to the energy pile-up. Such sensitivity decreases as the CFL σ is increased in the case of UWC-RK3 (see Figure 14);

(c) different order schemes of each family, namely WENO and UWC, provide a similar level of energy at $k_{1\%}^{\text{diff}}$, i.e. $E(k_{1\%}^{\text{diff}})$ is alike among them. In particular, the greatest coincidences are observed for 5-th and 7-th order UWC schemes, as well as for 5-th and 7-th order WENO schemes (see Figures 17 and 18). The 3-rd order version of such schemes seems significantly more diffusive;

(d) a good coincidence between the approximate dispersion-diffusion relation and the results for Burgers' turbulence is evidenced. The validity of the "1% rule" is assessed, showing that there are not larger cut-off percentages to define other rules that satisfy the properties above, i.e. items (a), (b) and (c) (see Figure 19);

(e) efficiency plots of the schemes have been presented (see Figure 7). These plots allow to make a choice of the spatial and temporal order of accuracy, as well as

of the CFL number, to obtain a sought value of $k_{1\%}^{\text{disp}}$ and/or $k_{1\%}^{\text{disp}}$, in terms of computational efficiency.

As stated by Maulik and San [40], the conclusions withdrawn for the forced Burgers' turbulence problem may not be smoothly extended to other more complex problems such as the Navier-Stokes equations and additional investigation/benchmarking would be required to verify the properties herein observed in such problems. Nonetheless, the reported observations may serve as guidelines for further studies for iLES when selecting high order finite volume numerical schemes.

Acknowledgments

This work was funded by the Spanish Ministry of Science and Innovation under the research project PGC2018-094341-B-I00 (Solán-Fustero, Navas-Montilla and García-Navarro). This work has also been partially funded by Gobierno de Aragón through Fondo Social Europeo (Feder 2014-2020 "Construyendo Europa desde Aragón") (Solán-Fustero, Navas-Montilla and García-Navarro).

Appendix A. WENO reconstruction coefficients

In this appendix values for the smoothness indicators, β_m, the optimal linear weights, d_m, and coefficients c_{mn} are shown. Their dimensions are determined by the spatial order of accuracy, K. For $K = 3$, we have:

$$\begin{aligned} &\beta_1 = (u_j - u_{j-1})^2 \qquad d^L = \frac{1}{3}\begin{pmatrix} 1 & 2 \end{pmatrix} \qquad c^L = \frac{1}{2}\begin{pmatrix} 3 & -1 \\ 1 & 1 \end{pmatrix} \\ &\beta_2 = (u_{j+1} - u_j)^2 \qquad d^R = \frac{1}{3}\begin{pmatrix} 2 & 1 \end{pmatrix} \qquad c^R = \frac{1}{2}\begin{pmatrix} 1 & 1 \\ -1 & 3 \end{pmatrix} \end{aligned} \tag{A.1}$$

For $K = 5$, we have:

$$\begin{aligned} \beta_1 &= \frac{13}{12}\left(u_{j-2} - 2u_{j-1} + u_j\right)^2 + \frac{1}{4}\left(u_{j-2} - 4u_{j-1} + 3u_j\right)^2 \\ \beta_2 &= \frac{13}{12}\left(u_{j-1} - 2u_j + u_{j+1}\right)^2 + \frac{1}{4}\left(u_{j-1} - u_{j+1}\right)^2 \\ \beta_3 &= \frac{13}{12}\left(u_j - 2u_{j+1} + u_{j+2}\right)^2 + \frac{1}{4}\left(3u_j - 4u_{j+1} + u_{j+2}\right)^2 \end{aligned} \tag{A.2}$$

$$\begin{aligned} &d^L = \frac{1}{10}\begin{pmatrix} 1 & 6 & 3 \end{pmatrix} \qquad c^L = \frac{1}{6}\begin{pmatrix} 11 & -7 & 2 \\ 2 & 5 & -1 \\ -1 & 5 & 2 \end{pmatrix} \\ &d^R = \frac{1}{3}\begin{pmatrix} 3 & 6 & 1 \end{pmatrix} \qquad c^R = \frac{1}{6}\begin{pmatrix} 2 & 5 & -1 \\ -1 & 5 & 2 \\ 2 & -7 & 11 \end{pmatrix} \end{aligned} \tag{A.3}$$

For $K = 7$, we have:

$$
\begin{aligned}
d^L &= \frac{1}{35}\begin{pmatrix} 1 & 12 & 18 & 4 \end{pmatrix} \qquad c^L = \frac{1}{12}\begin{pmatrix} 25 & -23 & 13 & -3 \\ 3 & 12 & -5 & 1 \\ -1 & 7 & 7 & -1 \\ 1 & -5 & 13 & 3 \end{pmatrix} \\
d^R &= \frac{1}{35}\begin{pmatrix} 4 & 18 & 12 & 1 \end{pmatrix} \qquad c^R = \frac{1}{12}\begin{pmatrix} 3 & 13 & -5 & 1 \\ -1 & 7 & 7 & -1 \\ 1 & -5 & 13 & 3 \\ -3 & 13 & -23 & 25 \end{pmatrix}
\end{aligned}
\tag{A.4}
$$

$$
\begin{aligned}
\beta_1 &= u_{j-3}\left(547u_{j-3} - 3882u_{j-2} + 4642u_{j-1} - 1854u_j\right) \\
&\quad + u_{j-2}\left(7043u_{j-2} - 17246u_{j-1} + 7042u_j\right) \\
&\quad + u_{j-1}\left(11003u_{j-1} - 9402u_j\right) + u_j\left(2107u_j\right) \\
\beta_2 &= u_{j-2}\left(267u_{j-2} - 1642u_{j-1} + 1602u_j - 494u_{j+1}\right) \\
&\quad + u_{j-1}\left(2843u_{j-1} - 5966u_j + 1922u_{j+1}\right) \\
&\quad + u_j\left(3443u_j - 2522u_{j+1}\right) + u_{j+1}\left(547u_{j+1}\right) \\
\beta_3 &= u_{j-1}\left(547u_{j-1} - 2522u_j + 1922u_{j+1} - 494u_{j+2}\right) \\
&\quad + u_j\left(3443u_j - 5966u_{j+1} + 1602u_{j+2}\right) \\
&\quad + u_{j+1}\left(2843u_{j+1} - 1642u_{j+2}\right) + u_{j+2}\left(267u_{j+2}\right) \\
\beta_4 &= u_j\left(2107u_j - 9402u_{j+1} + 7042u_{j+2} - 1854u_{j+3}\right) \\
&\quad + u_{j+1}\left(11003u_{j+1} - 17246u_{j+2} + 4642u_{j+3}\right) \\
&\quad + u_{j+1}\left(7043u_{j+2} - 3882u_{j+3}\right) + u_{j+3}\left(547u_{j+3}\right)
\end{aligned}
\tag{A.5}
$$

Appendix B. Dispersion-diffusion analysis of 2D WENO schemes

The method of Pirozzoli has been applied to obtain the dispersion-diffusion characteristics of the 2D spatial reconstruction schemes. Two different schemes have been considered for this analysis, namely the Class A and Class B WENO schemes detailed in [56]. On the one hand, the Class A reconstruction scheme is is based on a dimensional splitting, being faster and easier to implement at the cost of a reduction of the order of accuracy. On the other hand, the Class B scheme is based on a dimension-by-dimension 2D reconstruction and retains the formal order of accuracy, being more complicated in implementation. The approximate diffusion-dispersion errors of the Class A and the Class B semi-discrete schemes have been computed by applying the method of Pirozolli

method to the 2D advection equation:

$$\frac{\partial u}{\partial t} + \frac{\partial u}{\partial x} + \frac{\partial u}{\partial y} = 0, \tag{B.1}$$

in the domain $\Omega = [-L, L] \times [-L, L]$ and with initial condition $u(x, 0) = \hat{u}_k e^{i(k_x x + k_y y)}$, where k_x and k_y are the x and y wavenumbers. Cartesian grid and diagonal wave propagation direction have been considered.

The dispersion-diffusion curves for the WENO3-RK3, WENO5-RK3 and WENO7-RK3 schemes, computed for the semi-discrete case (i.e. $\sigma = 0$), are presented in Figures B.20, B.21 and B.22, respectively. A detail of the dispersion curves is shown in Figure B.23. The results show that differences between the 1D and 2D schemes are minor. The largest differences are observed in the dispersion curve, where the Class B 2D scheme shows a small deviation from the 1D curve.

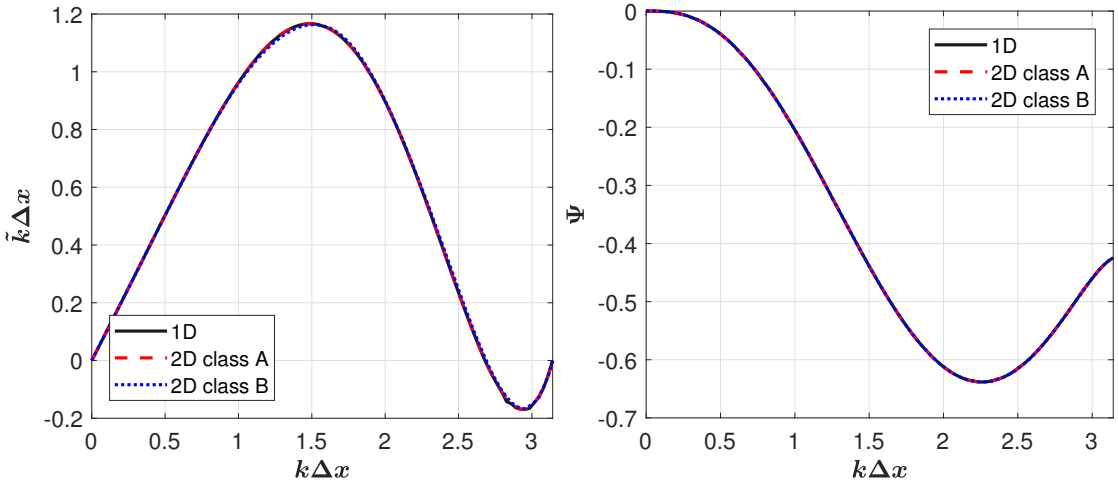

(a) Dispersion (semidiscrete, CFL=0.001).

(b) Diffusion (semidiscrete, CFL=0.001).

Figure B.20: 1D, 2D class A and 2D class B WENO3-RK3 [56] dispersion and diffusion characteristics.

Appendix C. Energy deviation criterion

We propose a simple criterion to detect the magnitude of the deviation of the computed spectrum at the wavenumbers given by the "1% rule" (due to an energy pile-up or due to excessive diffusion) with respect to the extrapolated inertial range:

1. Calculate the slope of the energy cascade (inertial region) of the computed solution, χ, by means of the least square method, allowing to define the extrapolated energy spectrum $E_\chi = k^{-\chi}$.
2. Compute the energy value in $k_{1\%}$ using the previous extrapolation $E_{\chi 1\%} = E_\chi(k_{1\%})$.
3. Finally, calculate the logarithmic difference between the energy of the computed solution at $k_{1\%}$ and the extrapolated energy magnitude as follows:

$$\Lambda = \log_{10} E(k_{1\%}) - \log_{10} E_{\chi 1\%} = \log_{10} \left(\frac{E(k_{1\%})}{E_{\chi 1\%}} \right). \tag{C.1}$$

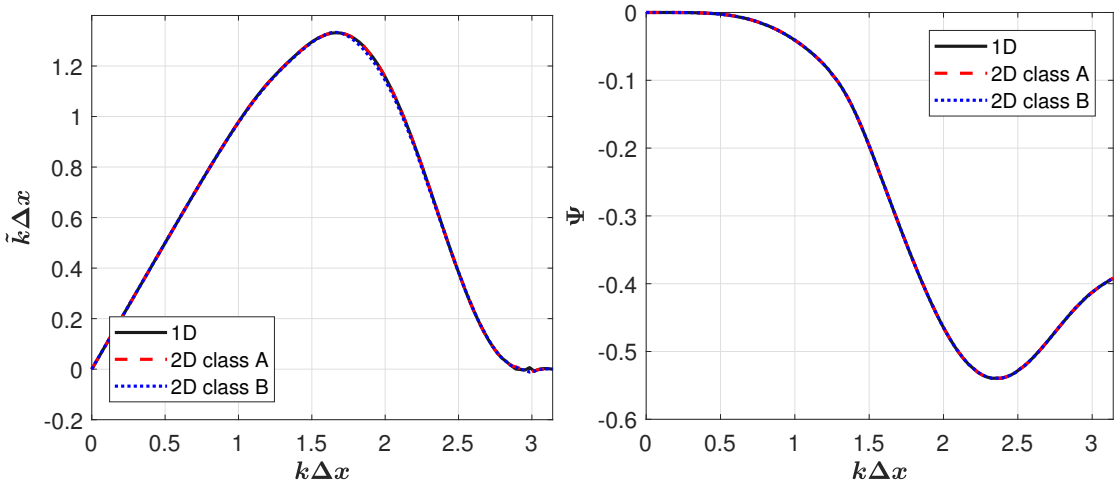

(a) Dispersion (semidiscrete, CFL=0.001). (b) Diffusion (semidiscrete, CFL=0.001).

Figure B.21: 1D, 2D class A and 2D class B WENO5-RK3 [56] dispersion and diffusion characteristics.

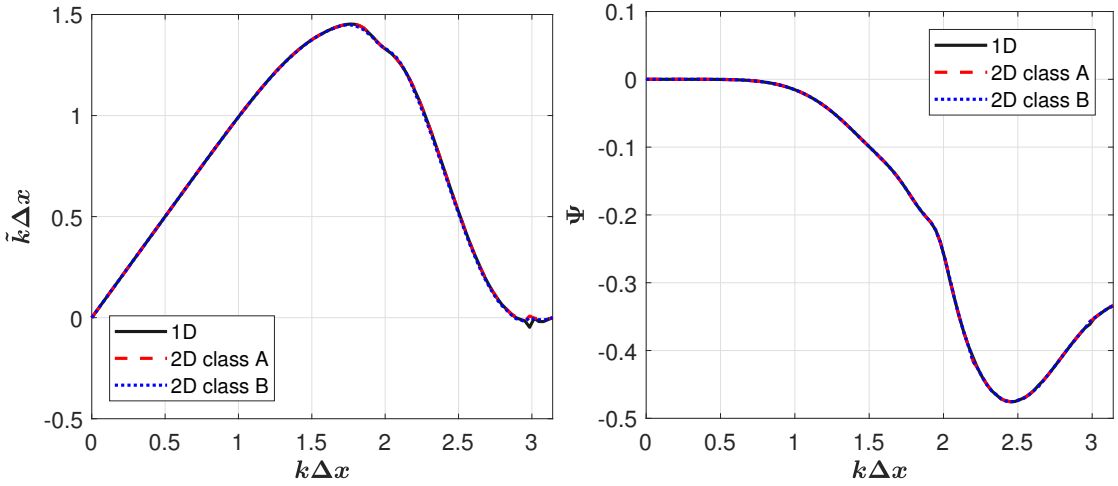

(a) Dispersion (semidiscrete, CFL=0.001). (b) Diffusion (semidiscrete, CFL=0.001).

Figure B.22: 1D, 2D class A and 2D class B WENO7-RK3 [56] dispersion and diffusion characteristics.

The presence or the absence of the energy pile-up will be denoted by the sign of Λ. This quantity will be computed using both dispersion and diffusion wavenumbers, $k_{1\%}^{\text{disp}}$ and $k_{1\%}^{\text{diff}}$, yielding to Λ^{disp} and Λ^{diff}. Figure C.24 shows an example of the extrapolation, $E_\chi(k_{1\%}^{\text{diff}})$, as well as the least square linear trend, $E_\chi(k)$, and the energy cascade of the numerical solution, $E(k)$. In this particular case, $E_\chi(k_{1\%}^{\text{diff}})$ lies beneath the extrapolated trend for the UWC3-RK3 scheme, i.e. $\Lambda^{\text{diff}} < 0$, and it lies above the extrapolated trend for the UWC7-RK3 scheme, i.e. $\Lambda^{\text{diff}} > 0$.

It must be pointed out that we have used the extrapolation of the inertial range of the computed spectrum instead of the ideal k^{-2} trend as it allows to measure relative variations with respect to the inertial range provided by each scheme.

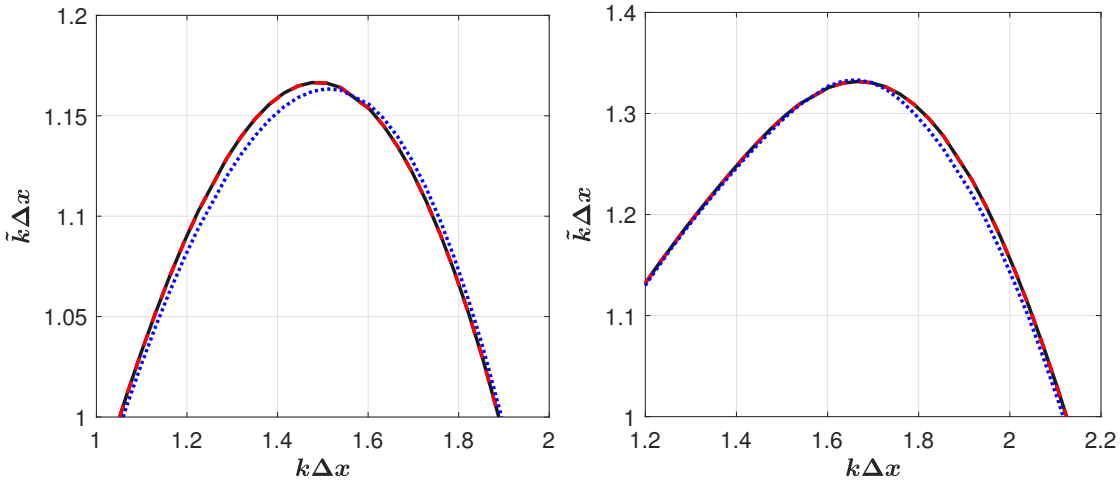

(a) Dispersion (semidiscrete, CFL=0.001).

(b) Dispersion (semidiscrete, CFL=0.001).

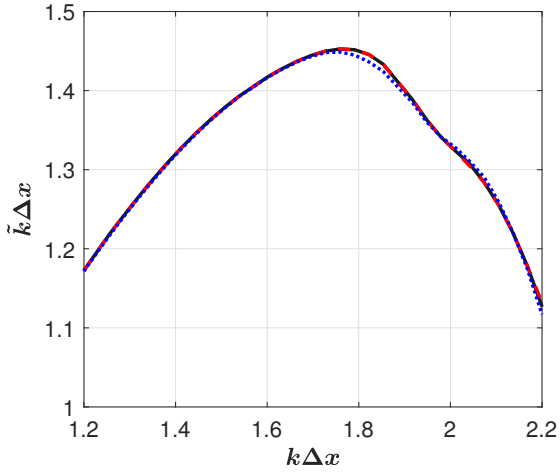

(c) Dispersion (semidiscrete, CFL=0.001).

Figure B.23: Zoom of 1D, 2D class A and 2D class B WENO3-RK3 [56] dispersion relation.

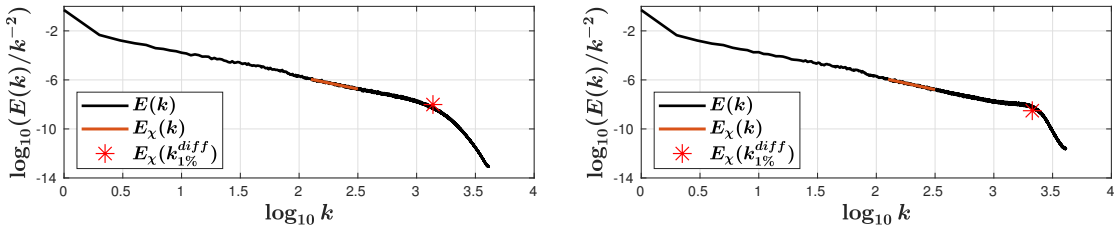

(a) UWC3-RK3.

(b) UWC7-RK3.

Figure C.24: Variables involved in the application of the pile-up criterion

Appendix D. Burgers' turbulence analysis with RK4 schemes

In this appendix the most relevant results obtained with UWC-RK4 schemes have been included. Figure D.25 shows the energy cascades of UWC-RK4 schemes with $\sigma = 0.5$ and 0.9, because the energy pile-up does not decrease, as it does in the UWC-RK3 results. For smaller values of the CFL number, $\sigma < 0.5$, the energy cascades for both set of schemes are very similar.

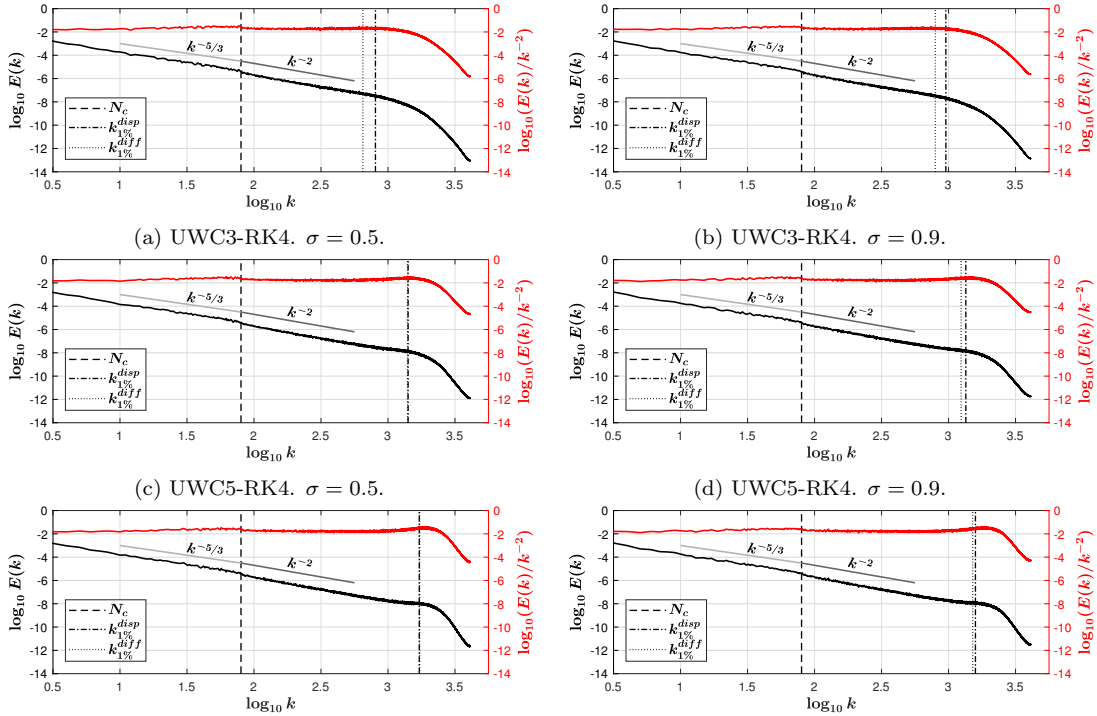

(a) UWC3-RK4. $\sigma = 0.5$.

(b) UWC3-RK4. $\sigma = 0.9$.

(c) UWC5-RK4. $\sigma = 0.5$.

(d) UWC5-RK4. $\sigma = 0.9$.

(e) UWC7-RK4. $\sigma = 0.5$.

(f) UWC7-RK4. $\sigma = 0.9$.

Figure D.25: Energy cascades for UWC-RK4 schemes, with $\sigma = 0.5$ and $\sigma = 0.9$. $N_c = 80$, $N = 8192$.

In Figure D.26, $k_{1\%}^{\text{disp}}$ and $k_{1\%}^{\text{disp}}$ values are represented alongside the wavenumber associated to the maximum pile-up.

Finally, Figure D.27 shows the results of the energy deviation criterion for the UWC-RK4.

References

[1] M. Alhawwary and Z. Wang, *Fourier analysis and evaluation of DG, FD and compact difference methods for conservation laws*, Journal of Computational Physics, 373 (2018), pp. 835 – 862, https://doi.org/https://doi.org/10.1016/j.jcp.2018.07.018, http://www.sciencedirect.com/science/article/pii/S0021999118304790.

[2] M. A. Alhawwary and Z. J. Wang, *A study of DG methods for diffusion using the combined-mode analysis*, https://doi.org/10.2514/6.2019-1157, https://arc.aiaa.org/doi/abs/10.2514/6.2019-1157, https://arxiv.org/abs/https://arc.aiaa.org/doi/pdf/10.2514/6.2019-1157.

[3] D. S. Balsara, *Higher-order accurate space-time schemes for computational astrophysics—Part I: finite volume methods*, Living Reviews in Computational Astrophysics, 3 (2017), https://doi.org/10.1137/070679065, https://doi.org/10.1007/s41115-017-0002-8, https://arxiv.org/abs/10.1007/s41115-017-0002-8.

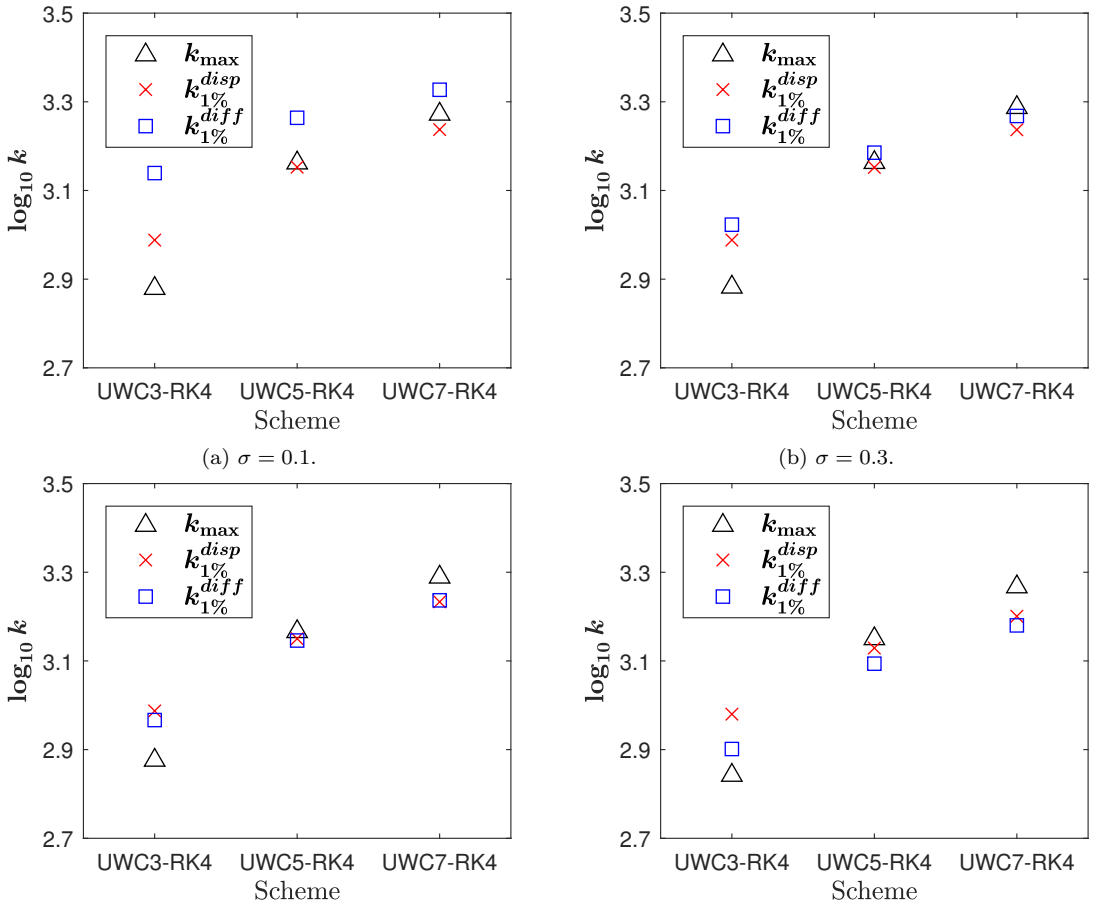

(a) $\sigma = 0.1$.

(b) $\sigma = 0.3$.

(c) $\sigma = 0.5$.

(d) $\sigma = 0.9$.

Figure D.26: Assessment of the coincidence of $k_{1\%}^{\text{disp}}$ and $k_{1\%}^{\text{diff}}$ with the positions of the pile-up maximum for UWC-RK4 schemes. Fixed data: $N_c = 80$ - $N = 8192$.

[4] D. S. Balsara, S. Garain, V. Florinski, and W. Boscheri, *An efficient class of WENO schemes with adaptive order for unstructured meshes*, Journal of Computational Physics, 404 (2020), p. 109062, https://doi.org/https://doi.org/10.1016/j.jcp.2019.109062, http://www.sciencedirect.com/science/article/pii/S0021999119307673.

[5] D. S. Balsara, S. Garain, and C.-W. Shu, *An efficient class of WENO schemes with adaptive order*, Journal of Computational Physics, 326 (2016), pp. 780 – 804, https://doi.org/https://doi.org/10.1016/j.jcp.2016.09.009, http://www.sciencedirect.com/science/article/pii/S0021999116304211.

[6] D. S. Balsara and C.-W. Shu, *Monotonicity preserving weighted essentially non-oscillatory schemes with increasingly high order of accuracy*, Journal of Computational Physics, 160 (2000), pp. 405 – 452, https://doi.org/https://doi.org/10.1006/jcph.2000.6443, http://www.sciencedirect.com/science/article/pii/S002199910096443X.

[7] J. Bec and K. Khanin, *Burgers turbulence*, Physics Reports, 447 (2007), p. 1–66, https://doi.org/10.1016/j.physrep.2007.04.002, http://dx.doi.

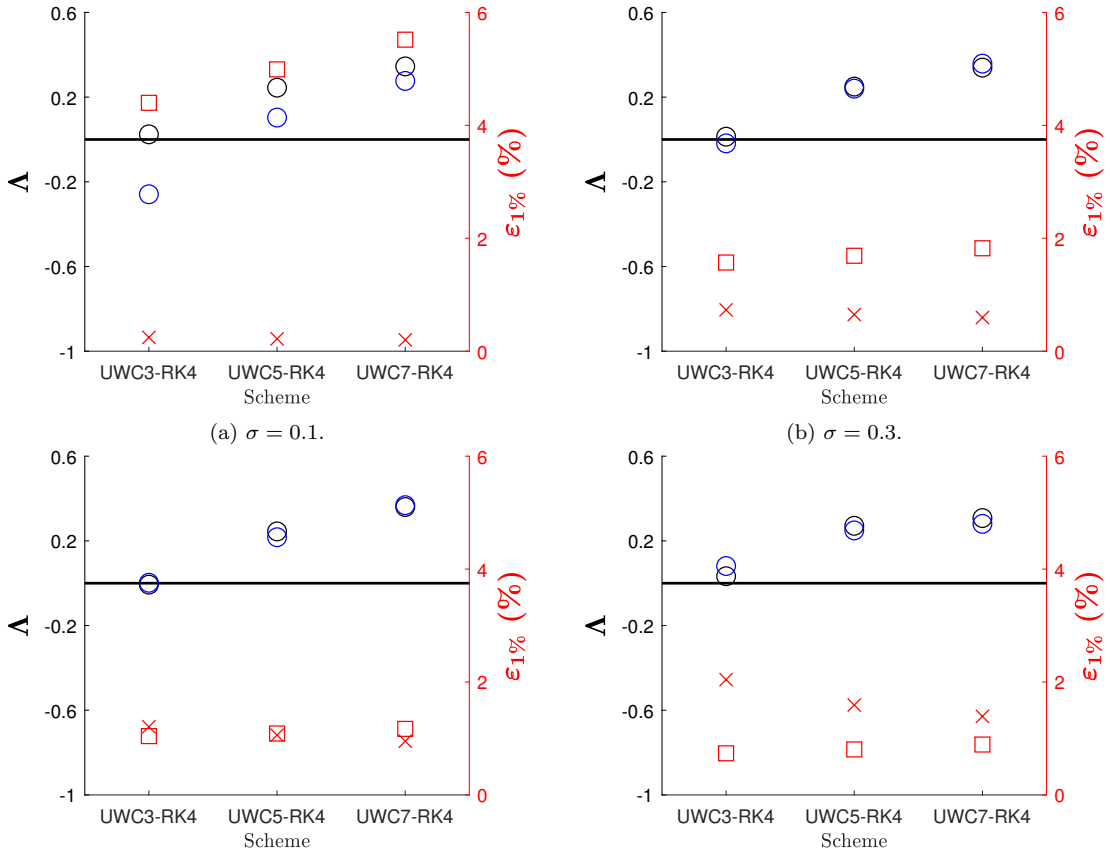

(a) $\sigma = 0.1$.

(b) $\sigma = 0.3$.

(c) $\sigma = 0.5$.

(d) $\sigma = 0.9$.

Figure D.27: Energy pile-up criterion for UWC-RK4 schemes, with $\sigma = 0.1$, $\sigma = 0.3$, $\sigma = 0.5$ and $\sigma = 0.9$. Contents: (—) $\Lambda = 0$, ◯ Λ^{disp}, ◯ Λ^{diff}, □ Dispersion error (%) y × Diffusion error (%). Fixed data: $N_c = 80$ - $N = 8192$.

org/10.1016/j.physrep.2007.04.002.

[8] C. Bogey and C. Bailly, *Large eddy simulations of round free jets using explicit filtering with/without dynamic Smagorinsky model*, International Journal of Heat and Fluid Flow, 27 (2006), pp. 603 – 610, https://doi.org/https://doi.org/10.1016/j.ijheatfluidflow.2006.02.008, http://www.sciencedirect.com/science/article/pii/S0142727X06000300. Special Issue of The Fourth International Symposium on Turbulence and Shear Flow Phenomena - 2005.

[9] R. Borges, M. Carmona, B. Costa, and W. S. Don, *An improved weighted essentially non-oscillatory scheme for hyperbolic conservation laws*, Journal of Computational Physics, 227 (2008), pp. 3191 – 3211, https://doi.org/https://doi.org/10.1016/j.jcp.2007.11.038, http://www.sciencedirect.com/science/article/pii/S0021999107005232.

[10] J. Burgers, *A mathematical model illustrating the theory of turbulence*, vol. 1 of Advances in Applied Mechanics, Elsevier, 1948, pp. 171 – 199, https://doi.org/https://doi.org/10.1016/S0065-2156(08)70100-5, http://www.sciencedirect.com/science/article/pii/S0065215608701005.

[11] M. Chavez-Modena, E. Ferrer, and G. Rubio, *Improving the stability of multiple-relaxation lattice Boltzmann methods with central moments*, Computers & Fluids, 172 (2018), pp. 397 – 409, https://doi.org/https://doi.org/10.1016/j.compfluid.2018.03.084, http://www.sciencedirect.com/science/article/pii/S0045793018301889.

[12] A. Chekhlov and V. Yakhot, *Kolmogorov turbulence in a random-force-driven Burgers equation: Anomalous scaling and probability density functions*, Phys. Rev. E, 52 (1995), pp. 5681–5684, https://doi.org/10.1103/PhysRevE.52.5681, https://link.aps.org/doi/10.1103/PhysRevE.52.5681.

[13] J. Crank and P. Nicolson, *A practical method for numerical evaluation of solutions of partial differential equations of the heat-conduction type*, Mathematical Proceedings of the Cambridge Philosophical Society, 43 (1947), p. 50–67, https://doi.org/10.1017/S0305004100023197.

[14] M. Dumbser, C. Enaux, and E. F. Toro, *Finite volume schemes of very high order of accuracy for stiff hyperbolic balance laws*, Journal of Computational Physics, 227 (2008), pp. 3971 – 4001, https://doi.org/https://doi.org/10.1016/j.jcp.2007.12.005, http://www.sciencedirect.com/science/article/pii/S0021999107005578.

[15] L. M. . W. R. F. Grinstein, *Implicit Large Eddy Simulation: Computing Turbulent Fluid Dynamics*, Cambridge University Press, 2007, https://doi.org/10.1017/CBO9780511618604.

[16] G. Falkovich and K. R. Sreenivasan, *Lessons from Hydrodynamic Turbulence*, Physics Today, 59 (2006), p. 43, https://doi.org/10.1063/1.2207037.

[17] F. Fambri, M. Dumbser, and O. Zanotti, *Space–time adaptive ADER-DG schemes for dissipative flows: Compressible Navier–Stokes and resistive MHD equations*, Computer Physics Communications, 220 (2017), p. 297–318, https://doi.org/10.1016/j.cpc.2017.08.001, http://dx.doi.org/10.1016/j.cpc.2017.08.001.

[18] N. Fehn, W. Wall, and M. Kronbichler, *Efficiency of high-performance Discontinuous Galerkin spectral element methods for under-resolved turbulent incompressible flows*, International Journal for Numerical Methods in Fluids, 88 (2018), pp. 32–54, https://doi.org/10.1002/fld.4511, https://onlinelibrary.wiley.com/doi/abs/10.1002/fld.4511, https://arxiv.org/abs/https://onlinelibrary.wiley.com/doi/pdf/10.1002/fld.4511.

[19] E. Ferrer, *An interior penalty stabilised incompressible discontinuous Galerkin-Fourier solver for implicit large eddy simulations*, Journal of Computational Physics, 348 (2017), pp. 754–775, https://doi.org/https://doi.org/10.1016/j.jcp.2017.07.049, http://www.sciencedirect.com/science/article/pii/S0021999117305570.

[20] L. Fu, *A very-high-order TENO scheme for all-speed gas dynamics and turbulence*, Computer Physics Communications, 244 (2019), pp. 117 – 131, https://doi.org/https://doi.org/10.1016/j.cpc.2019.06.013, http://www.sciencedirect.com/science/article/pii/S0010465519302000.

[21] P. Garcia-Navarro and M. Vazquez-Cendon, *On numerical treatment of the source terms in the shallow water equations*, Computers & Fluids, 29 (2000), pp. 951 – 979, https://doi.org/https://doi.org/10.1016/S0045-7930(99)00038-9, http://www.sciencedirect.com/science/article/pii/S0045793099000389.

[22] E. Garnier, M. Mossi, P. Sagaut, P. Comte, and M. Deville, *On the use of shock-capturing schemes for large-eddy simulation*, Journal of Computational Physics, 153 (1999), pp. 273 – 311, https://doi.org/https://doi.org/10.1006/jcph.1999.6268, http://www.sciencedirect.com/science/article/pii/S002199919996268X.

[23] G. J. Gassner and A. D. Beck, *On the accuracy of high-order discretizations for underresolved turbulence simulations*, Theoretical and Computational Fluid Dynamics, 27 (2013), pp. 221–237, https://doi.org/10.1007/s00162-011-0253-7, https://doi.org/10.1007/s00162-011-0253-7.

[24] S. Gottlieb, Z. Grant, and D. Higgs, *Optimal explicit strong stability preserving Runge-Kutta methods with high linear order and optimal nonlinear order*, Mathematics of Computation, 84 (2014), https://doi.org/10.1090/mcom/2966.

[25] C. Hirsch, *The Analysis of Numerical Schemes*, in Numerical Computation of Internal and External Flows (Second Edition), C. Hirsch, ed., Butterworth-Heinemann, Oxford, second edition ed., 2007, pp. 279 – 281, https://doi.org/https://doi.org/10.1016/B978-075066594-0/50048-5, http://www.sciencedirect.com/science/article/pii/B9780750665940500485.

[26] F. Jia, Z. Gao, and W. S. Don, *A Spectral Study on the Dissipation and Dispersion of the WENO Schemes*, Journal of Scientific Computing, 63 (2014), https://doi.org/10.1007/s10915-014-9886-1.

[27] G.-S. Jiang and C.-W. Shu, *Efficient implementation of weighted ENO schemes*, Journal of Computational Physics, 126 (1996), pp. 202 – 228, https://doi.org/https://doi.org/10.1006/jcph.1996.0130, http://www.sciencedirect.com/science/article/pii/S0021999196901308.

[28] E. Johnsen, J. Larsson, A. V. Bhagatwala, W. H. Cabot, P. Moin, B. J. Olson, P. S. Rawat, S. K. Shankar, B. Sjögreen, H. Yee, X. Zhong, and S. K. Lele, *Assessment of high-resolution methods for numerical simulations of compressible turbulence with shock waves*, Journal of Computational Physics, 229 (2010), pp. 1213 – 1237, https://doi.org/https://doi.org/10.1016/j.jcp.2009.10.028, http://www.sciencedirect.com/science/article/pii/S0021999109005804.

[29] A. N. Kolmogorov, *The local structure of turbulence in incompressible viscous fluid for very large reynolds numbers*, Proceedings: Mathematical and Physical Sciences, 434 (1991), pp. 9–13, http://www.jstor.org/stable/51980.

[30] A. LaBryer, P. J. Attar, and P. Vedula, *A framework for large eddy simulation of Burgers turbulence based upon spatial and temporal statistical information*, Physics of Fluids, 27 (2015), p. 035116, https://doi.org/10.1063/1.4916132, https://doi.org/10.1063/1.4916132, https://arxiv.org/abs/https://doi.org/10.1063/1.4916132.

[31] R. J. LeVeque, *Finite Volume Methods for Hyperbolic Problems*, Cambridge Texts in Applied Mathematics, Cambridge University Press, 2002, https://doi.org/10.1017/CBO9780511791253.

[32] Y. Li and Z. Wang, *A priori and a posteriori evaluations of sub-grid scale models for the Burgers' equation*, Computers & Fluids, 139 (2016), pp. 92 – 104, https://doi.org/https://doi.org/10.1016/j.compfluid.2016.04.015, http://www.sciencedirect.com/science/article/pii/S0045793016301190. 13th USNCCM International Symposium of High-Order Methods for Computational Fluid Dynamics - A special issue dedicated to the 60th birthday of Professor David Kopriva.

[33] Y. Li, C. Yan, and J. Yu, *High accuracy schemes for compressible turbulence simulations*, 07 2017, pp. 239–243, https://doi.org/10.1109/ICMAE.2017.8038649.

[34] X.-D. Liu, S. Osher, and T. Chan, *Weighted Essentially Non-oscillatory Schemes*, Journal of Computational Physics, 115 (1994), pp. 200 – 212, https://doi.org/https://doi.org/10.1006/jcph.1994.1187, http://www.sciencedirect.com/science/article/pii/S0021999184711879.

[35] M. D. Love, *Subgrid modelling studies with Burgers' equation*, Journal of Fluid Mechanics, 100 (1980), p. 87–110, https://doi.org/10.1017/S0022112080001024.

[36] J. Manzanero, *Dispersion-diffusion analysis for variable coefficient advection problems, with application to alternative DG formulations and under-resolved turbulence.*, master's thesis, Universidad Politécnica de Madrid, 2016.

[37] J. Manzanero, E. Ferrer, G. Rubio, and E. Valero, *Design of a Smagorinsky spectral Vanishing Viscosity turbulence model for Discontinuous Galerkin methods*, Computers & Fluids, 200 (2020), p. 104440, https://doi.org/https://doi.org/10.1016/j.compfluid.2020.104440, http://www.sciencedirect.com/science/article/pii/S0045793020300165.

[38] J. Manzanero, G. Rubio, E. Ferrer, and E. Valero, *Dispersion-dissipation analysis for advection problems with nonconstant coefficients: Applications to Discontinuous Galerkin formulations*, SIAM Journal on Scientific Computing, 40 (2018), pp. A747–A768, https://doi.org/10.1137/16M1101143.

[39] R. Maulik and O. San, *Resolution and energy dissipation characteristics of implicit LES and explicit filtering models for compressible turbulence*, Fluids, 2 (2017), p. 14.

[40] R. Maulik and O. San, *Explicit and implicit LES closures for Burgers turbulence*, Journal of Computational and Applied Mathematics, 327 (2018), p. 12–40, https://doi.org/10.1016/j.cam.2017.06.003, http://dx.doi.org/10.1016/j.cam.2017.06.003.

[41] R. Moura, S. Sherwin, and J. Peiró, *Linear dispersion-diffusion analysis and its application to under-resolved turbulence simulations using Discontinuous Galerkin spectral/hp methods*, J. Comput. Phys., 298 (2015), pp. 695–710, https://doi.org/10.1016/j.jcp.2015.06.020, http://dx.doi.org/10.1016/j.jcp.2015.06.020.

[42] A. Navas-Montilla, C. Juez, M. Franca, and J. Murillo, *Depth-averaged unsteady RANS simulation of resonant shallow flows in lateral cavities using augmented WENO-ADER schemes*, Journal of Computational Physics, (2019), https://doi.org/10.1016/j.jcp.2019.06.037.

[43] A. Navas-Montilla and J. Murillo, *Energy balanced numerical schemes with very high order. the Augmented Roe Flux ADER scheme. Application to the shallow water equations*, Journal of Computational Physics, 290 (2015), pp. 188 – 218, https://doi.org/https://doi.org/10.1016/j.jcp.2015.03.002, http://www.sciencedirect.com/science/article/pii/S0021999115001217.

[44] S. Pirozzoli, *On the spectral properties of shock-capturing schemes*, J. Comput. Phys., 219 (2006), pp. 489–497, https://doi.org/10.1016/j.jcp.2006.07.009, http://dx.doi.org/10.1016/j.jcp.2006.07.009.

[45] S. B. Pope, *Turbulent Flows*, Cambridge University Press, 2000, https://doi.org/10.1017/CBO9780511840531.

[46] K. Ritos, I. W. Kokkinakis, and D. Drikakis, *Performance of high-order implicit large eddy simulations*, Computers & Fluids, 173 (2018), pp. 307 – 312, https://doi.org/https://doi.org/10.1016/j.compfluid.2018.01.030, http://www.sciencedirect.com/science/article/pii/S0045793018300380.

[47] O. San and K. Kara, *Evaluation of Riemann flux solvers for WENO reconstruction schemes: Kelvin–Helmholtz instability*, Computers & Fluids, 117 (2015), pp. 24 – 41, https://doi.org/https://doi.org/10.1016/j.compfluid.2015.04.026, http://www.sciencedirect.com/science/article/pii/S0045793015001486.

[48] O. San and A. E. Staples, *High-order methods for decaying two-dimensional homogeneous isotropic turbulence*, Computers & Fluids, 63 (2012), pp. 105 – 127, https://doi.org/https://doi.org/10.1016/j.compfluid.2012.04.006, http://www.sciencedirect.com/science/article/pii/S0045793012001363.

[49] N. Sharan, G. Matheou, and P. E. Dimotakis, *Mixing, scalar boundedness, and numerical dissipation in large-eddy simulations*, Journal of Computational Physics, 369 (2018), pp. 148 – 172, https://doi.org/https://doi.org/10.1016/j.jcp.2018.05.005, http://www.sciencedirect.com/science/article/pii/S0021999118302973.

[50] J. Shi, Y.-T. Zhang, and C.-W. Shu, *Resolution of high order WENO schemes for complicated flow structures*, Journal of Computational Physics, 186 (2003), pp. 690–696, https://doi.org/10.1016/S0021-9991(03)00094-9.

[51] C.-W. Shu, *Essentially non-oscillatory and weighted essentially non-oscillatory schemes for hyperbolic conservation laws*, Springer Berlin Heidelberg, Berlin, Heidelberg, 1998, https://doi.org/10.1007/BFb0096355, https://doi.org/10.1007/BFb0096355.

[52] C.-W. Shu, *High order weighted essentially nonoscillatory schemes for convection dominated problems*, SIAM Review, 51 (2009), pp. 82–126, https://doi.org/10.1137/070679065, https://doi.org/10.1137/070679065, https://arxiv.org/abs/https://doi.org/10.1137/070679065.

[53] V. Titarev and E. Toro, *ADER schemes for three-dimensional non-linear hyperbolic systems*, Journal of Computational Physics, 204 (2005), pp. 715 – 736, https://doi.org/https://doi.org/10.1016/j.jcp.2004.10.028, http://www.sciencedirect.com/science/article/pii/S0021999104004358.

[54] A. Uranga, P.-O. Persson, M. Drela, and J. Peraire, *Implicit large eddy simulation of transition to turbulence at low Reynolds numbers using a Discontinuous Galerkin method*, International Journal for Numerical Methods in Engineering, 87 (2011), pp. 232–261, https://doi.org/10.1002/nme.3036.

[55] B. C. Vermeire, S. Nadarajah, and P. G. Tucker, *Implicit large eddy simulation using the high-order correction procedure via reconstruction scheme*, International Journal for Numerical Methods in Fluids, 82 (2016), pp. 231–260, https://doi.org/10.1002/fld.4214, https://onlinelibrary.wiley.com/doi/abs/10.1002/fld.4214, https://arxiv.org/abs/https://onlinelibrary.wiley.com/doi/pdf/10.1002/fld.4214.

[56] R. Zhang, M. Zhang, and C.-W. Shu, *On the order of accuracy and numerical performance of two classes of finite volume WENO schemes*, Communications in Computational Physics, 9 (2011), p. 807–827, https://doi.org/10.4208/cicp.291109.080410s.

[57] S. Zhao, N. Lardjane, and I. Fedioun, *Comparison of improved finite-difference WENO schemes for the implicit large eddy simulation of turbulent non-reacting and reacting high-speed shear flows*, Computers & Fluids, 95 (2014), pp. 74 – 87, https://doi.org/https://doi.org/10.1016/j.compfluid.2014.02.017, http://www.sciencedirect.com/science/article/pii/S0045793014000802.